



Petrology and geochemistry of spinel peridotite xenoliths from Hannuoba and Qixia, North China craton

Roberta L. Rudnick^{a,*}, Shan Gao^{b,c}, Wen-li Ling^b,
Yong-shen Liu^b, William F. McDonough^a

^aGeochemistry Laboratory, Department of Geology, University of Maryland, College Park, MD 20742, USA

^bFaculty of Earth Sciences, China University of Geosciences, Wuhan 430074, China

^cKey Laboratory of Continental Dynamics, Department of Geology, Northwest University, Xi'an 710069, China

Received 27 June 2003; accepted 17 February 2004

Available online 25 May 2004

Abstract

We report mineralogical and chemical compositions of spinel peridotite xenoliths from two Tertiary alkali basalt localities on the Archean North China craton (Hannuoba, located in the central orogenic block, and Qixia, in the eastern block). The two peridotite suites have major element compositions that are indistinguishable from each other and reflect variable degrees (0–25%) of melt extraction from a primitive mantle source. Their compositions are markedly different from typical cratonic lithosphere, consistent with previous suggestions for removal of the Archean mantle lithosphere beneath this craton. Our previously published Os isotopic results for these samples [Earth Planet. Sci. Lett. 198 (2002) 307] show that lithosphere replacement occurred in the Paleoproterozoic beneath Hannuoba, but in the Phanerozoic beneath Qixia. Thus, we see no evidence for a compositional distinction between Proterozoic and Phanerozoic continental lithospheric mantle. The Hannuoba xenoliths equilibrated over a more extensive temperature (hence depth) interval than the Qixia xenoliths. Neither suite shows a correlation between equilibration temperature and major element composition, indicating that the lithosphere is not chemically stratified in either area. Trace element and Sr and Nd isotopic compositions of the Hannuoba xenoliths reflect recent metasomatic overprinting that is not related to the Tertiary magmatism in this area.

© 2004 Elsevier B.V. All rights reserved.

Keywords: Peridotite xenolith; Archean craton; North China craton; Major and trace element geochemistry; Sr and Nd isotopes; Thermometry

1. Introduction

Archean cratons are underlain by mantle lithosphere that is thick, cold and refractory (Jordan, 1975, 1988; van der Hilst and McDonough, 1999). Such lithosphere has a high viscosity because it is cold and nearly

anhydrous, and thus contributes significantly to craton stability (Pollack, 1986; Hirth et al., 2000). However, not all regions of Archean-aged crust are underlain by such refractory mantle lithosphere, and these regions are characterized by a more protracted history of tectonism and magmatism than their cratonic counterparts. There are at least two possible reasons for the absence of thick mantle keels beneath Archean-aged crust: (1) they may have never formed, or (2) they may have formed but were subsequently removed.

* Corresponding author. Tel.: +1-301-405-1311.

E-mail address: rudnick@geol.umd.edu (R.L. Rudnick).

An example of the first possibility is the Mojave terrain in SW U.S. Here, the crust has Paleoproterozoic to late Archean Nd model ages (Bennett and DePaolo, 1987; Raymo and Calzia, 1998) but middle Proterozoic crystallization ages (Wooden and Miller, 1990). Mojavia is underlain by late Archean lithospheric mantle that is considerably more fertile and dense than typical cratonic mantle (Lee et al., 2001). Hence, this mantle lithosphere did not grow to the same thickness as that beneath Archean cratons. Lee et al. (2001) proposed that the thinner lithosphere beneath Mojavia failed to shield this small fragment of Archean lithosphere from tectonic reworking. This study demonstrated that thick lithospheric keels do not always form beneath Archean crust.

An example of the second possibility is the North China craton, where multiple lines of evidence (surface geology, xenolith studies, seismic and heat flow data) show that this craton formed with a thick lithospheric keel in the Archean that was subsequently removed (e.g., Menzies et al., 1993; Griffin et al., 1998). The timing and

mechanisms of lithospheric mantle removal beneath the North China craton are yet to be fully understood.

The present paper reports the petrography, mineral chemistry, thermometry and major element compositions of spinel peridotite xenoliths from the Hannuoba and Qixia localities for which Os data have previously been reported (Gao et al., 2002). In addition, for the Hannuoba peridotites, we present trace element and Sr and Nd isotope geochemistry. We show that the Sr and Nd isotopes reflect recent metasomatic overprinting not related to the Tertiary hosts and that both Hannuoba and Qixia peridotites are indistinguishable in terms of their bulk compositions, despite the fact that their formation ages differ by nearly 2 billion years.

2. Geologic setting

The North China craton is divided into three regions based on geology, tectonic evolution and P – T – t paths

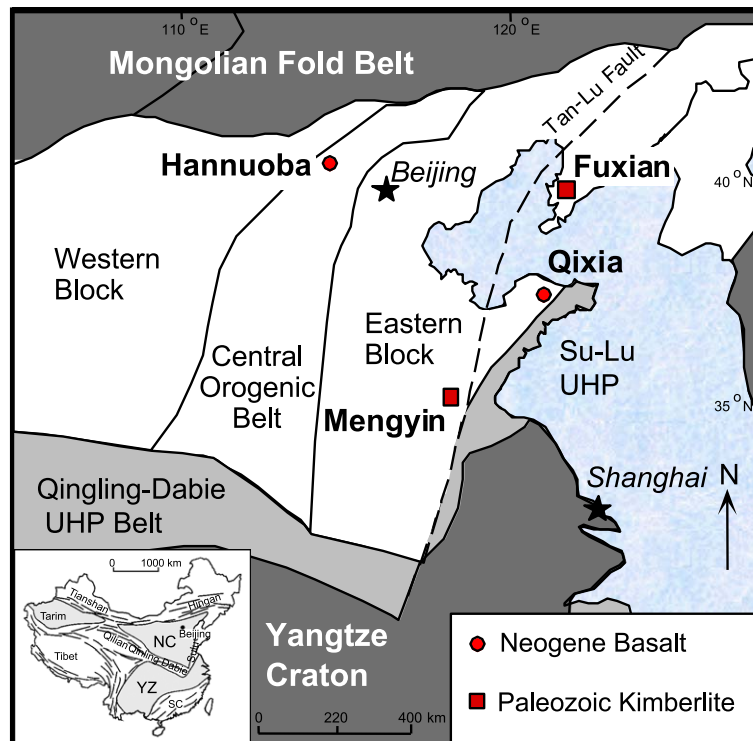


Fig. 1. Map of North China craton (white) showing xenolith localities mentioned in the text. Tectonic subdivisions are based on Zhao et al. (2000, 2001). Inset shows location of the North China craton (NC) relative to other cratonic blocks (e.g., YZ—Yangtze craton) and intervening fold belts.

of metamorphic rocks (Fig. 1; Kusky et al., 2001; Zhao et al., 2000, 2001). The western block forms a stable platform composed of late Archean to Paleoproterozoic metasedimentary belts that unconformably overly Archean basement (Wu et al., 1998; Li et al., 2000; Zhao et al., 2000). The latter consists of granulite facies tonalite–trondhjemite–granodiorite (TTG) gneiss and charnockite (3300 Ma; Kröner et al., 1987) with minor mafic granulite and amphibolite. The Central Orogenic Belt, or Trans-North China orogen, separates the western and eastern blocks of the craton. This belt is composed of late Archean amphibolites and granulites and 2500 Ma granite–greenstone terrains (Kröner et al., 1988; Kern et al., 1996; Zhao et al., 2000, 2001). These are overlain by Paleoproterozoic bimodal volcanic rocks in the southern part of the orogen and thick carbonate and terrigenous sedimentary rocks intercalated with basaltic flows in the central part of the orogen; these deposits may reflect a continental rift

setting during the Paleoproterozoic. The basement of the eastern block of the North China craton is composed of early to late Archean orthogneisses intruded by 2500 Ma syntectonic granitoids (Zhao et al., 2000, 2001). A variety of geochronological and P – T – t evidence, cited in Zhao et al. (2000, 2001), document a major collisional event between the eastern and western blocks of the North China craton between 1800 and 2000 Ma. This event formed the Central Orogenic Belt and represents the final amalgamation of the North China craton.

Unlike other Archean cratons, the North China craton experienced widespread tectonothermal reactivation during the late Mesozoic and Cenozoic. This is documented by the emplacement of voluminous Mesozoic granitic and volcanic rocks (Qiu et al., 2002; Yang et al., 2003), which were followed by extensive Tertiary basaltic volcanism. The latter carries a variety of mantle and crustal xenoliths (Cao and Zhu, 1987),

Table 1
Major and trace element analysis of basalt standards at Northwest University in Xi'an

	BCR-2						GSR-3					
	Meas.	1 σ	<i>n</i>	RSD (%)	Rec.	RE (%)	Meas.	1 σ	<i>n</i>	RSD (%)	Rec.	RE (%)
SiO ₂ (wt.%)	54.0	0.2	4	0.45	54.1	0.16	44.6	0.02	3	0.05	44.64	–0.10
TiO ₂	2.26	0.02	4	0.91	2.26	0.11	2.40	0.03	3	1.20	2.37	–1.13
Al ₂ O ₃	13.4	0.08	4	0.57	13.5	1.00	13.86	0.10	3	0.74	13.83	0.24
Fe ₂ O ₃ ^a	13.9	0.04	4	0.29	13.8	–0.36	13.29	0.08	3	0.63	13.40	–0.85
MnO	0.183	0.005	4	2.74	0.19	3.95	0.16	0.01	3	3.53	0.17	–3.92
MgO	3.69	0.01	4	0.27	3.59	–2.65	7.79	0.04	3	0.49	7.77	0.21
CaO	7.17	0.02	4	0.24	7.12	–0.67	8.81	0.03	3	0.30	8.81	0
Na ₂ O	3.10	0.10	4	3.34	3.16	1.98	3.47	0.09	3	2.49	3.38	2.56
K ₂ O	1.80	0.01	4	0.28	1.79	–0.70	2.31	0.02	3	0.66	2.32	–0.29
P ₂ O ₅	0.35	0	4	0	0.35	0	0.94	0.01	3	0.61	0.95	–0.70
V (ppm)	445	19	3	4.18	416	–7.05	200	1	3	0.58	167	19.96
Cr	60	1	3	1.94	18	–231	125	7	3	5.31	134	–6.47
Co	50	2	3	3.08	37	–34	54	2	3	2.81	46.5	16.85
Ni	27	1	3	4.33			137	1	3	0.73	140	–2.14
Zn	128	17	3	13.5	127	–1.05	151	2	3	1.01	150	0.44
Ga	23	1	3	4.35	23	0	24	1	3	4.17	24.8	–3.23
Rb	48.7	0.6	3	1.19	48	–1.39	38.7	0.6	3	1.49	37	4.50
Sr	330	2	3	0.61	346	4.62	1104	12	3	1.08	1100	0.33
Y	32	1	3	3.65	37	14.4	23	3	3	13.48	22	3.03
Zr	179	2	3	1.16	188	4.61	290	1	3	0.50	277	4.69

BCR-2G and GSR-3 are USGS and Chinese National standards, respectively.

n: number of analyses; Meas.: measured value; Rec.: recommended value; RSD: relative standard deviation; RE: relative error between measured and recommended values.

Recommended values are from http://minerals.cr.usgs.gov/geo_chem_stand/ and Govindaraju (1994).

^a All Fe reported as Fe₂O₃.

some of which are the focus of this paper. The region also experienced the development of extensive sedimentary basins (most of the eastern portion of the craton is covered by Quaternary sediments) and presently has high heat flow (60 mW/m²; Hu et al., 2000) compared to other Archean cratons (Nyblade et al., 1990). The changes in tectonic and magmatic activity are also reflected in a change in mantle xenolith

compositions (Menzies et al., 1993; Griffin et al., 1998); xenoliths carried in Ordovician kimberlites are deep-seated garnet-facies peridotites that are highly refractory, like cratonic xenoliths elsewhere. These xenoliths record the presence of a cold and thick lithospheric keel, consistent with the occurrence of diamonds in the kimberlites. In contrast, xenoliths carried in the Tertiary alkali basalts derive from shal-

Table 2

Analyses of USGS basalt (BHVO-1) and andesite (AGV-1) standards by ICP–MS at the Xi'an laboratory

Isotope	Blank	BHVO-1 (<i>n</i> =2)					AGV-1 (<i>n</i> =2)					
		Meas.	1 σ	RSD (%)	Rec.	RE (%)	Meas.	1 σ	RSD (%)	Rec.	RE (%)	
Li	6	99	5.08	0.17	3.4	4.6	10.4	10.5	0.34	3.2	12.0	-12.4
Be	9	4	0.99	0.01	0.8	1.1	-10.4	2.21	0.06	2.7	2.1	5.2
Sc	45	32	31.8	0.07	0.2	31.8	-0.2	12	0.06	0.5	12.2	1.1
V	51	903	314	0.17	0.1	317	-0.9	122	0.38	0.3	121	0.8
Cr	52	604	285	5	1.8	289	-1.2	12	0.13	1.1	10.1	19.3
Co	59	55	45	0.29	0.6	45	0.2	15	0.08	0.5	15.3	-0.6
Ni	60	146	121	3.35	2.8	121	-0.1	15	1.68	11.1	16	-5.7
Cu	65	131	138	0.65	0.5	136	1.8	56	0.48	0.8	60	-6.6
Zn	66	260	110	0.68	0.6	105	4.4	80	0.25	0.3	88	-8.8
Ga	71	30	21	0.06	0.3	21	0.5	20.3	0.15	0.7	20	1.4
Ge	74	11	1.65	0.03	1.6	1.64	0.4	1.28	0.04	3.3	1.25	2.6
Rb	85	219	9.6	0.13	1.4	11	-12.6	66	0.18	0.3	67.3	-2.3
Sr	88	458	399	2.06	0.5	403	-0.9	662	1.33	0.2	662	0.001
Y	89	30	27.3	0.05	0.2	27.6	-1.2	21	0.09	0.4	20	5.3
Zr	90	263	173	0.67	0.4	179	-3.6	233	0.87	0.4	227	2.5
Nb	93	32	19.3	0.07	0.4	19	1.4	15	0.1	0.4	15	-1.3
Cs	133	10	0.11	0.01	6.0	0.13	-12.9	1.34	0.01	0.4	1.28	5.0
Ba	135	559	138	0.32	0.2	139	-0.8	1234	8	0.6	1226	0.6
La	139	102	15.6	0.05	0.3	15.8	-1.5	38.4	0.11	0.3	38	1.1
Ce	140	135	38.3	0.01	0.0	39	-1.7	68.4	0.10	0.1	67	2.1
Pr	141	25	5.44	0.02	0.4	5.7	-4.6	8.4	0.03	0.4	7.6	10.9
Nd	146	107	25.6	0.10	0.4	25.2	1.6	32.8	0.07	0.2	33	-0.6
Sm	147	27	6.24	0.03	0.5	6.2	0.7	5.9	0.04	0.7	5.9	-0.8
Eu	151	3	2.01	0.01	0.4	2.06	-2.2	1.69	0.02	1.0	1.64	2.8
Gd	157	25	6.17	0.06	1.0	6.4	-3.7	5.40	0.05	0.8	5	8.0
Tb	159	3	0.96	0.003	0.4	0.96	-0.2	0.70	0.0001	0.0	0.7	0.1
Dy	161	5	5.20	0.01	0.1	5.2	0.0	3.63	0.01	0.3	3.6	0.7
Ho	165	3	0.98	0.003	0.3	0.99	-1.1	0.68	0.01	1.4	0.67	1.1
Er	166	5	2.36	0.01	0.5	2.4	-1.6	1.75	0.03	1.8	1.7	3.1
Tm	169	3	0.32	0.002	0.6	0.33	-2.7	0.25	0.0004	0.2	0.34	-26
Yb	172	6	2.03	0.02	1.0	2.02	0.6	1.70	0.02	1.4	1.72	-1.0
Lu	175	5	0.30	0.0001	0.0	0.29	4.1	0.26	0.01	2.5	0.27	-2.1
Hf	178	10	4.41	0.03	0.6	4.38	0.6	5.10	0.03	0.6	5.1	-0.02
Ta	181	3	1.23	0.005	0.4	1.23	0.1	0.90	0.01	0.7	0.90	-0.4
Pb	208	123	2.33	0.11	4.7	2.6	-10.5	36.3	0.7	1.9	36	0.8
Th	232	7	1.25	0.02	1.2	1.08	16.0	6.39	0.05	0.8	6.5	-1.6
U	238	4	0.42	0.01	1.4	0.42	0.8	1.88	0.02	1.3	1.92	-2.2

n: number of analyses; Meas.: measured value; Rec.: recommended value; RSD: relative standard deviation; RE: relative error between measured and recommended values.

Recommended values are from http://minerals.cr.usgs.gov/geo_chem_stand/ and Govindaraju (1994).

Table 3
Major and trace element data for Hannuoba and Qixia spinel lherzolite xenoliths

Sample	SiO ₂	TiO ₂	Al ₂ O ₃	Cr ₂ O ₃	FeO	MnO	NiO	MgO	CaO	Na ₂ O	K ₂ O	P ₂ O ₅	Total	Mg#			
<i>Hannuoba peridotites</i>																	
DMP-04	44.40	0.06	2.29		7.33	0.13	0.31	42.05	1.94	0.28	0.015	0.010	98.79	91.1			
DMP-05	44.15	0.13	2.83	0.36	7.53	0.13	0.31	41.55	2.18	0.26	0.020	0.010	99.46	90.8			
DMP-19	44.83	0.03	1.91	0.34	7.07	0.12	0.31	40.74	1.80	0.19	0.025	0.010	97.35	91.1			
DMP-23a	44.22	0.10	2.32	0.42	7.77	0.13	0.31	41.25	1.64	0.24	0.100	0.030	98.53	90.4			
DMP-25	44.39	0.08	1.61	0.36	7.11	0.12	0.31	43.88	1.00	0.30	0.135	0.030	99.32	91.7			
DMP-41	44.75	0.06	2.76	0.40	7.74	0.13	0.26	40.15	2.12	0.27	0.004	0.011	98.67	90.2			
DMP-51	44.83	0.05	1.96	0.38	7.41	0.12	0.29	41.97	1.89	0.24	0.006	0.003	99.14	91.0			
DMP-56	44.79	0.13	3.49	0.35	7.97	0.14	0.26	38.15	3.21	0.36	0.007	0.006	98.85	89.5			
DMP-56-rep.	44.59	0.16	3.73	0.34	7.84	0.13	0.27	38.47	3.03	0.28	0.020	0.010	98.87	89.7			
DMP-57	44.34	0.06	1.96	0.37	7.41	0.12	0.32	42.47	1.56	0.16	0.020	0.010	98.79	91.1			
DMP-58	44.87	0.08	3.16	0.34	7.92	0.13	0.27	38.82	2.76	0.34	0.012	0.005	98.72	89.7			
DMP-59	43.99	0.06	2.58	0.40	7.99	0.13	0.29	40.38	2.43	0.27	0.007	0.019	98.54	90.0			
DMP-60	46.34	0.11	3.67	0.38	7.48	0.13	0.25	36.68	3.47	0.38	0.006	0.009	98.90	89.7			
DMP-60	45.92	0.14	3.90	0.39	7.41	0.13	0.28	37.20	3.24	0.35	0.020	0.015	98.99	89.9			
DMP-67c	44.00	0.20	3.78	0.42	8.39	0.14	0.26	37.81	2.88	0.30	0.260	0.020	98.46	88.9			
KD-03	44.45	0.11	3.08	0.37	7.70	0.13	0.29	41.05	2.31	0.28	0.020	0.010	99.80	90.5			
KD-04	44.23	0.14	3.29	0.34	8.01	0.14	0.27	40.29	2.47	0.32	0.023	0.010	99.53	90.0			
<i>Qixia peridotites</i>																	
Q1	44.15	0.09	2.56		8.21	0.14		39.94	2.79	0.30	0.064	0.064	98.31	89.7			
Q4	44.48	0.10	3.52		7.83	0.13		38.54	3.23	0.32	0.111	0.047	98.31	89.8			
Q5	43.94	0.04	1.61		7.83	0.13		43.63	1.08	0.11	0.011	0.020	98.38	90.9			
Q6	43.27	0.01	1.02		7.87	0.13		45.15	0.54	0.11	0.010	0.007	98.12	91.1			
Q8	44.30	0.01	1.44		7.64	0.13		42.23	1.95	0.06	0.057	0.129	97.94	90.8			
Q17	44.18	0.13	3.40	0.35	8.35	0.14	0.24	38.36	2.98	0.33	0.095	0.034	98.23	89.1			
QX-07	42.72	0.11	3.41	0.42	7.96	0.13	0.29	40.07	2.45	0.28	0.130	0.070	97.62	90.0			
QX-09	41.43	0.02	4.01	0.44	7.56	0.13	0.32	43.40	1.11	0.09	0.040	0.010	98.12	91.1			
QX-11	43.59	0.10	2.99	0.34	8.12	0.13	0.29	40.80	2.52	0.30	0.080	0.020	98.94	90.0			
QX-13	43.83	0.11	3.09	0.42	7.95	0.13	0.29	39.99	2.53	0.23	0.040	0.060	98.25	90.0			
QX-14	45.22	0.02	2.13	0.46	7.23	0.13	0.29	41.44	1.59	0.18	0.120	0.010	98.36	91.1			
Sample	C	S	S dup	Li	Be	Sc	Ti	V	V	Cr	Cr	Co	Ni	Ni	Cu	Zn	Zn
								(XRF)		(XRF)			(XRF)			(XRF)	
<i>Hannuoba peridotites</i>																	
DMP-04	272	73		1.64	0.018	12.7		70	51	2739	2477	106	2429	2322	17	57	37
DMP-05	243	5	203					63		2466			2407			64	
DMP-19	1729	91	46	2.34	0.059	10.1		25	39	2322	2238	108	2413	2454	10	37	33
DMP-23A				4.22	0.16	10.6		55	45	2879	2814	103	2432	2432	9	85	56
DMP-25	1202	20	25	2.41	0.105	10.0		41	38	2466	2318	108	2462	2377	10	53	35
DMP-41	283	110		1.55	0.028	12.9	357	52	59	2751	2654	105	2071	2224	15	53	40
DMP-51	264	130		1.85	0.030	11.9	238	43	49	2620	2619	107	2257	2403	14.7	50	36
DMP-56	280	260		2.23	0.043	16.2	715	67	74	2372	2318	103	2029	2006	27.3	57	42
DMP-56-rep.								88		2342			2145			56	
DMP-57	248	70	53					56		2509			2509			49	
DMP-58	184	230		2.13	0.027	14.9	417	57	65	2343	2224	103	2112	2190	20.5	53	38
DMP-59	294	200		2.09	0.049	12.8	357	50	55	2727	2628	110	2307	2366	20.8	56	42
DMP-60	245	320		2.20	0.021	17.2	596	68	75	2579	2530	97	1949	1967	22.4	51	39
DMP-60								85		2690			2209			69	
DMP-67C	183	23	35	4.67	0.16	16.0		83	73	2880	2634	99	2046	2120	12.5	76	54
KD-03	136	17	4					65		2526			2271				53
KD-04								80		2325			2144				59

(continued on next page)

Table 3 (continued)

Sample	C	S	S dup	Li	Be	Sc	Ti	V (XRF)	V	Cr (XRF)	Cr	Co	Ni (XRF)	Ni	Cu	Zn (XRF)	Zn
<i>Qixia peridotites</i>																	
Q1	472	72															
Q4	439	66															
Q5	316	26															
Q6																	
Q8	744	65															
Q17	198	38					780	63		2394			1912				54
QX-07	208	18						68		2853			2254				61
QX-09								27		2991			2529				54
QX-11	199	9						59		2300			2303				56
QX-13								82		2843			2249				59
QX-14								62		3143			2256				51
Sample	Ga (XRF)	Ga	Ge	Rb (XRF)	Rb	Sr (XRF)	Sr	Y (XRF)	Y	Zr (XRF)	Zr	Nb	Cs	Ba	La	Ce	Pr
<i>Hannuoba peridotites</i>																	
DMP-04		2.1	0.9		0.28		4.38		1.46	2.16		0.18	0.008	0.77	0.141	0.35	0.050
DMP-05																	
DMP-19		2.97	0.91		0.81		17.9		0.73	3.43		0.73	0.011	1.40	0.23	0.51	0.068
DMP-23A		2.63	0.92		2.04		43.2		1.99	9.45		2.79	0.042	16.01	2.04	5.08	0.73
DMP-25		1.35	0.92		2.07		17.7		0.80	6.24		2.08	0.005	13.82	2.27	3.56	0.42
DMP-41	8	8.44	0.9	b.d.	0.15	6	6.27	1.8	1.93	3	2.84	0.26	0.003	0.364	0.77	1.40	0.16
DMP-51	2	1.91	0.94	0.20	0.73	4	4.23	1.3	1.3	2	2.27	0.18	0.026	1.20	0.21	0.40	0.075
DMP-56	4	3.73	1.03	0.30	0.35	11	9.83	3.5	3.7	7	6.72	0.49	0.009	0.78	0.17	0.59	0.116
<i>DMP-56-rep.</i>																	
DMP-57																	
DMP-58	3	3.14	0.98	0.50	0.46	5	4.57	2.6	2.7	2	2.57	0.35	0.013	0.545	0.088	0.19	0.037
DMP-59	2	2.39	0.96	0.40	0.44	9	8.31	1.8	1.9	3	3.20	0.53	0.020	3.25	1.32	2.02	0.22
DMP-60	3	3.13	1.08	0.20	0.26	16	15	3.3	3.7	5	5.14	0.22	0.005	5.26	3.06	1.09	0.087
DMP-60																	
DMP-67C		4.62	1.05		4.19		29.7		4.23		15.3	1.23	0.009	16.43	1.24	3.38	0.52
KD-03																	
KD-04																	
<i>Qixia peridotites</i>																	
Q1																	
Q4																	
Q5																	
Q6																	
Q8																	
Q17	4			1.9		45		3.2		8							
QX-07																	
QX-09																	
QX-11																	
QX-13																	
QX-14																	
Sample	Nd	Sm	Eu	Gd	Tb	Dy	Ho	Er	Tm	Yb	Lu	Hf	Ta	Pb	Th	U	
<i>Hannuoba peridotites</i>																	
DMP-04	0.26	0.10	0.036	0.13	0.030	0.20	0.050	0.14	0.025	0.18	0.031	0.101	0.012	0.116	b.d.	0.005	
DMP-05																	
DMP-19	0.31	0.074	0.031	0.09	0.016	0.11	0.025	0.08	0.013	0.09	0.017	0.087	0.029	0.318	0.013	0.062	
DMP-23A	3.59	0.82	0.26	0.71	0.10	0.48	0.080	0.18	0.023	0.15	0.024	0.26	0.14	0.296	0.149	0.045	

Table 3 (continued)

DMP-25	1.71	0.34	0.086	0.29	0.040	0.17	0.028	0.062	0.009	0.060	0.010	0.22	0.11	0.190	0.278	0.058
DMP-41	0.68	0.17	0.062	0.21	0.045	0.30	0.070	0.20	0.032	0.24	0.040	0.15	0.013	0.145	0.015	0.031
DMP-51	0.38	0.13	0.040	0.15	0.031	0.20	0.050	0.14	0.028	0.17	0.034	0.19	0.011	0.172	0.018	0.014
DMP-56	0.74	0.29	0.11	0.38	0.09	0.58	0.14	0.37	0.061	0.41	0.069	0.28	0.009	0.144	b.d.	0.015
DMP-56-rep.																
DMP-57																
DMP-58	0.25	0.15	0.061	0.22	0.057	0.40	0.10	0.29	0.049	0.34	0.055	0.13	0.011	0.133	b.d.	0.029
DMP-59	0.88	0.20	0.062	0.23	0.045	0.29	0.072	0.21	0.034	0.24	0.041	0.14	0.022	0.167	0.072	0.023
DMP-60	0.50	0.24	0.10	0.36	0.082	0.57	0.14	0.40	0.062	0.45	0.075	0.22	0.008	0.220	0.642	0.062
DMP-60																
DMP-67C	2.64	0.74	0.24	0.75	0.14	0.82	0.16	0.44	0.066	0.43	0.071	0.50	0.081	0.514	0.115	0.041
KD-03																
KD-04																
<i>Qixia peridotites</i>																
Q1																
Q4																
Q5																
Q6																
Q8																
Q17																
QX-07																
QX-09																
QX-11																
QX-13																
QX-14																

Major elements as wt.% oxides. FeO as total Fe, originally measured as Fe₂O₃ and converted to FeO. Trace elements in micrograms per gram. Sample numbers listed in italics show samples for which XRF data are from the Xi'an lab, all others are from the University of Massachusetts.

lower depths, are relatively hot and have less refractory compositions. Collectively, these observations indicate the loss of ~ 80–140 km of Archean lithosphere from beneath the eastern portion of the North China craton.

Our previously published Os results (Gao et al., 2002) show evidence for two episodes of replacement of Archean lithospheric mantle. One episode occurred during the Paleoproterozoic beneath the Trans-North China orogen, as the Hannuoba peridotites yield a Paleoproterozoic (1.9 Ga) Re–Os age that overlaps the period of cratonization documented by Zhao et al. (2000, 2001). In contrast, and as predicted from earlier studies (Menzies et al., 1993; Griffin et al., 1998), thick Archean lithosphere persisted under the eastern block of the North China craton through the Ordovician. Garnet peridotite xenoliths carried in the Fuxian kimberlite pipe record Archean Re depletion ages (Gao et al., 2002). The single sample from Mengyin yielded a Mesoproterozoic Re depletion age, but the relatively high Re/Os of this sample suggests disturbance to the Re–Os system. This ancient lithosphere was replaced

after the Ordovician by mantle lithosphere that has Os isotopic characteristics indistinguishable from modern convecting upper mantle, as observed in xenoliths from Qixia (Gao et al., 2002).

3. Samples and previous work

The samples investigated here are spinel-facies peridotites from the Hannuoba and Qixia xenolith localities (Fig. 1). In this section, we review the xenolith associations at each locality and some results from previous investigations. A more complete discussion of previous results for the peridotite xenoliths, in the context of our new data, is provided in Sections 6 and 7.

3.1. Hannuoba

The Hannuoba basalts (10–22 Ma; Zhu, 1998) carry a remarkable variety of deep-seated xenoliths from both the lower crust and upper mantle. These include

mafic to felsic granulites (Gao et al., 2000; Chen et al., 2001; Liu et al., 2001; Zhou et al., 2002; Wilde et al., 2003), spinel- and garnet-bearing pyroxenites (Song and Frey, 1989; Tatsumoto et al., 1992; Chen et al., 2001; Xu, 2002), abundant spinel lherzolites and harzburgites (Song and Frey, 1989; Tatsumoto et al., 1992; Fan et al., 2000; Chen et al., 2001) and rare spinel–garnet lherzolites (Fan and Hooper, 1989; Chen et al., 2001).

Although mafic granulites dominate the granulite xenolith populations, intermediate and felsic granulites are common and metapelite xenoliths are also present. The mafic and intermediate granulites are cumulates interpreted to have formed by magmatic underplating and subsequent fractional crystallization at the base of the crust (Chen et al., 2001; Liu et al., 2001; Zhou et al., 2002), possibly during the Mesozoic, based on zircon U–Pb ages (Fan et al., 1998; Liu et al., 2001). However, more recently, Wilde et al. (2003) suggested that the Phanerozoic zircons in the granulite xenoliths are metamorphic in origin and the granulite protoliths are Precambrian. Liu et al. (2004) found oscillatory-zoned igneous zircon in an olivine pyroxenite to be Mesozoic,

suggesting that the melts that gave rise to the pyroxenites provided the heat to metamorphose the lower crust. The estimated lower crust composition, based on xenolith and geophysical studies, is intermediate (Gao et al., 2000; Liu et al., 2001).

Garnet pyroxenites yield a narrow P – T range (1.6–1.9 GPa, 990–1030 °C) that reflects an elevated geotherm (Chen et al., 2001). However, the narrow pressure window makes its shape difficult to define. The Hannuoba pyroxenites have been variably interpreted as metamorphic segregations (Chen et al., 2001) or young (late Mesozoic) cumulates from basaltic magmas (Xu, 2002). The distinctive trace element patterns of some Al-pyroxenites (Eu anomalies, high field-strength element depletions), coupled with their very wide range of Nd and Sr isotopic compositions, are interpreted to reflect mixing between mantle and crustal sources to generate the basalts from which the pyroxenites precipitated (Xu, 2002).

The samples investigated here are all spinel-facies peridotites from the Damaping (DMP) locality in the Hannuoba basalt field. They range in size from 10 to 35 cm and in composition from lherzolite to harzburgite

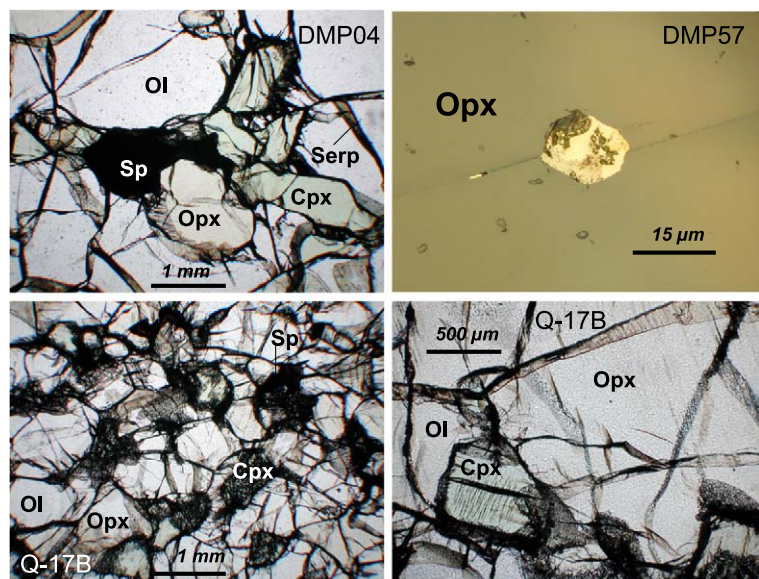


Fig. 2. Photomicrographs of representative textures of Hannuoba and Qixia spinel-facies peridotites. Upper panels: Hannuoba lherzolite DMP-04 (left) shows typical granuloblastic texture of Hannuoba xenoliths and serpentinite along grain boundary (plane polarized light). Primary sulfide (monosulfide solid solution) within orthopyroxene in lherzolite DMP-57 (right), reflected light. Lower panels (plane polarized light): Qixia lherzolite QX-17B (left) shows breakdown texture of clinopyroxene, whereas right panel shows a large orthopyroxene porphyroblast adjacent to clinopyroxene and olivine. Both pyroxenes contain exsolution lamellae.

(i.e., <5% clinopyroxene). Although composite xenoliths are relatively common at Hannouba, none of the samples investigated here contain any pyroxenite veins. Os isotope results for these samples demonstrate that they formed ~ 1.9 Ga ago as residues of partial melting (Gao et al., 2002). Trace element and Sr, Nd and Pb isotopic compositions of clinopyroxene separates reflect later metasomatic overprinting (Song and Frey, 1989; Tatsumoto et al., 1992; see Discussion).

3.2. Qixia

In contrast to Hannouba, mantle xenoliths from the 9–18 Ma Qixia olivine nephelinites have re-

ceived less attention (Fan and Hooper, 1989; Zheng et al., 1998), perhaps because of their relatively small size <6 cm and comparative scarcity. In addition to spinel-facies peridotites, the Qixia nephelinite also carries clinopyroxenites (Zheng et al., 1998) and olivine websterites (Fan et al., 2000), the latter of which can be considerably Fe-rich ($Fe_{0.83}$) and have evolved Sr and Nd isotopic compositions ($^{143}Nd/^{144}Nd=0.51141$, $^{87}Sr/^{86}Sr=0.70956$; Fan et al., 2000). Trace element patterns of clinopyroxenes have been used to infer the origin of the spinel peridotites as residues of up to 20% fractional melting, followed by metasomatic enrichment of the highly incompatible elements, perhaps by carbo-

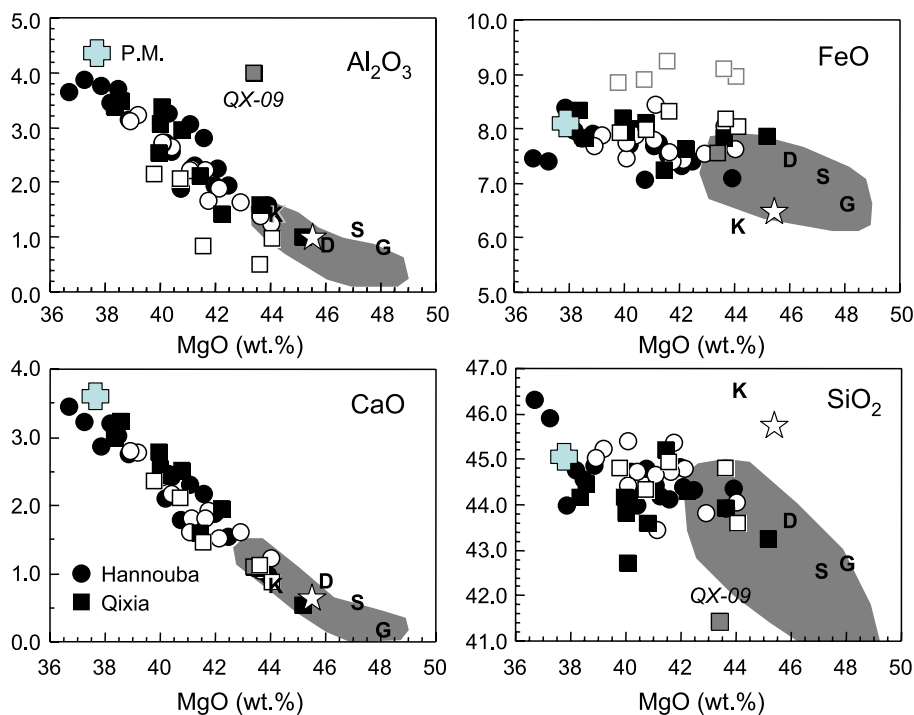


Fig. 3. Major element compositional variations for peridotite xenoliths investigated here. Circles are data for Hannouba spinel peridotites: \circ represent previously published data (Song and Frey, 1989; Chen et al., 2001); \bullet are data from this study. \blacksquare are data from Qixia xenoliths (this study) and \square are previously published data (Zheng et al., 1998). The iron data published by Zheng et al. is reported as FeO. However, if true, these samples would plot significantly above all others on the MgO vs. FeO plot (shown as faint gray squares). We assume that the data are in fact Fe_2O_3 and have plotted the data accordingly. One Qixia xenolith from this study (QX-09, gray symbol) shows an anomalously high Al_2O_3 content and low SiO_2 content, reflecting an overabundance of spinel in the mode. Cross denotes primitive mantle (P.M.) from McDonough and Sun (1995). Gray field represents cratonic peridotite xenoliths from the Tanzanian craton (Lee and Rudnick, 1999). These do not show the extensive metasomatic overprints that are more typical of cratonic peridotites from the Kaapvaal craton (including orthopyroxene enrichment; Boyd, 1989). Averages for other cratons given by letters: K: Kaapvaal (Boyd, 1989); D: Daldyn, Siberia; S: Slave (both from Griffin et al., 1999); G: east Greenland (from Bernstein et al., 1998); \star represents average "Archon" from Griffin et al. (1999).

natites (Zheng et al., 1998). These results are discussed further in Discussion in the context of the new data presented here.

The Qixia xenoliths investigated here are spinel lherzolites, harzburgites and a unique dunite. All xenoliths are found within the host lava, most of which are only relatively thin veneers of peridotite on an exposed weathering surface. The size of the xenoliths investigated here is small, ranging from 2 to 5 cm. The dunite (QX-18), which consists entirely of mosaic textured olivine, has an extremely forsteritic olivine composition (FO_{98} , Table 4). The origin of this unusual sample is unclear and it is not discussed further in this paper. Re–Os investigations of the spinel-facies peridotites show them to have $^{187}\text{Os}/^{188}\text{Os}$ that is indistinguishable from modern convecting mantle (Gao et al., 2002), consistent with

recent (Mesozoic or younger) formation of this section of lithospheric mantle.

4. Analytical methods

The xenoliths were sawn from their lava hosts and the cut surfaces were abraded with quartz in a sand blaster to remove any possible contamination from the saw blade. The samples were then disaggregated between thick plastic sheets with a rock hammer and reduced to powder using first an alumina disk mill followed by an alumina ring mill. A portion of the crushed fraction was sieved and clinopyroxene separates were handpicked under a binocular microscope to a purity of >98%. They were cleaned in an ultrasonic bath in distilled water before isotopic analysis.

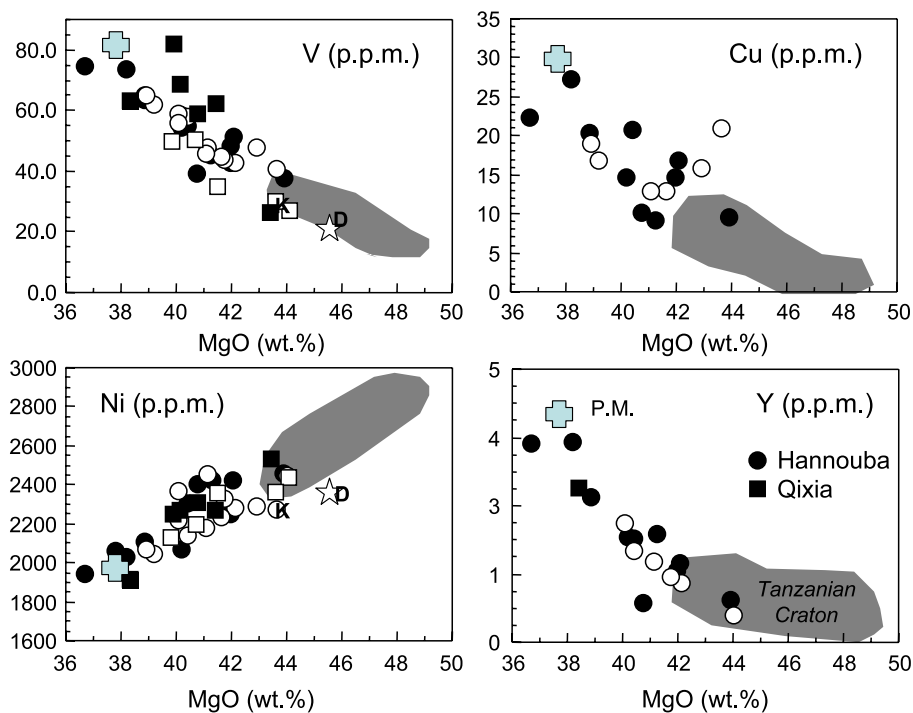


Fig. 4. Compatible and moderately incompatible trace element compositional variations for the peridotite xenoliths investigated here. Circles are data for Hannouba spinel peridotites: ○ represent previously published data (Song and Frey, 1989; Chen et al., 2001); ● are data from this study. ■ are data from Qixia xenoliths (this study) and □ are previously published data (Zheng et al., 1998). Cross denotes primitive mantle (P.M.) from McDonough and Sun (1995). Gray field represents cratonic peridotite xenoliths from the Tanzanian craton (Lee and Rudnick, 1999). Averages for other cratons given by letters: K: Kaapvaal; D: Daldyn (Griffin et al., 1999); and ☆ represents average "Archon" from Griffin et al. (1999).

Mineral analyses were carried out on polished thick sections both at Harvard University, using a Camebax MBX electron microprobe (EMP), and at the University of Maryland on a JEOL 8900 Electron Probe Microanalyzer. Analyses on the Camebax were performed in wavelength dispersive mode with 15 keV accelerating voltage and a 15 nA beam current. Samples analysed at the University of Maryland Laboratory for Microscopy and Microanalysis utilized the following operating conditions: 15 keV accelerating voltage, 20 nA cup current and a 5–10 μm beam. Natural standards were used for the analysis of olivine (Fe, Mg, Ni and Si—San Carlos olivine; Al and Ca—Kakanui hornblende; Mn—Rockport fayalite), pyroxene (Mn and Fe—Rockport fayalite; Mg and Ni—San Carlos olivine; Cr—Johnstown hypersthene; Ca—Mammoth Lakes wollastonite; Al—augite; Na and Ti—Kakanui hornblende) and chromite (Cr, Mn and Si—Bushveld chromite; Mg, Al and Fe—spinel). Raw intensities were corrected using the Bence–Albee (olivine) and CIT–ZAF (chromite and pyroxene) algorithms.

Major element compositions of whole rocks were determined by XRF on fused glass disks at the University of Massachusetts at Amherst (see Rhodes, 1996, for analytical details) and Northwest University in Xi'an, China. Samples analysed in the latter laboratory are designated with italicized labels in Table 3. Selected trace elements (V, Cr, Ni, Zn, Rb, Sr, Y and Zr) were also determined on pressed powder pellets by XRF in both laboratories. Accuracy and precision of the XRF data from the Xi'an lab can be evaluated from results obtained for USGS standard BCR-2 and Chinese National standard GSR-3 (Table 1). Precision (RSD) is better than 6% for the major and trace elements. Accuracy, as indicated by relative difference (RE) between measured and recommended values, is better than 4% for major elements and 14% for most of the trace elements. The only exceptions are Cr and Co in BCR-2, whose measured values are significantly higher than the recommended values for this standard, by a factor of 230% and 34%, respectively. Both elements are in low concentration in BCR-2; the correspondence between measured and recommended values is better for GSR-3, which has higher concen-

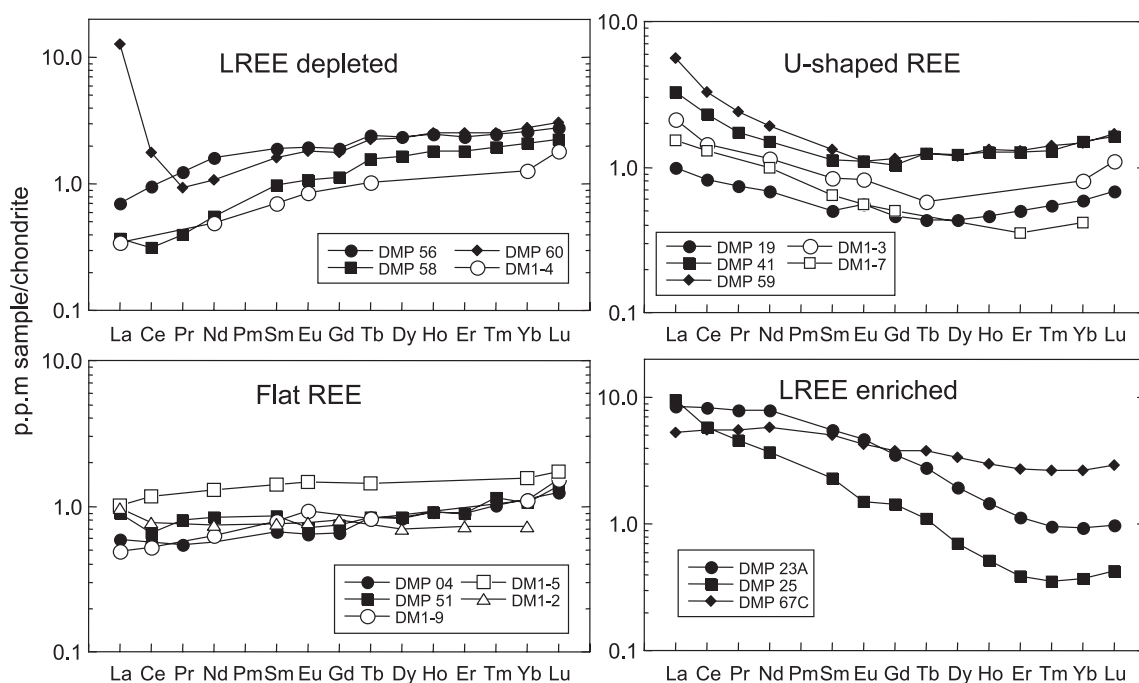


Fig. 5. Chondrite-normalized REE patterns for Hannuoba whole rock peridotites. Filled symbols are data from this work and open symbols are data from Song and Frey (1989). Chondrite values from McDonough and Sun (1995).

trations of both elements. Moreover, the close correspondence between peridotite Cr values obtained in both XRF laboratories and between the XRF and ICP–MS data (Table 3 and discussion below), leads us to conclude that the Xi'an XRF Cr values for the peridotites are accurate to within 10%.

Whole rock trace element compositions were determined by ICP–MS (Elan 6100 DRC) after acid digestion of samples in Teflon bombs at Northwest University, Xi'an, China. Table 2 shows results for two USGS standards (BHVO-1 and AGV-1) analysed in this laboratory during the course of these analyses. Based on these analyses, precision is generally better than 5% for most elements and accuracy is better than 10%, with many elements agreeing to within 2% of the reference values. Exceptions are Rb, Cs and Th in BHVO-1 (which differ by up to 16%) and Cr and Tm in AGV-1, which differ by up to 26% from the reference values. The Tm value we obtained for AGV-1 (0.25 ppm) is significantly lower than the

recommended value (0.34 ppm); the latter is probably in error, based on the positive Tm anomaly created by this value in the chondrite-normalized rare earth element (REE) pattern for AGV-1. The higher Cr values we obtained for AGV-1 may reflect polyatomic interferences (e.g., $^{36}\text{Ar}^{16}\text{O}$ on ^{52}Cr). However, a similar discrepancy in Cr data is not observed for BHVO-1, which has a higher Cr content. With the exception of Zn, elemental concentrations determined by both XRF and ICP–MS (V, Cr, Ni, Ga, Rb, Sr, Y and Zr) agree to within 10% (Table 3).

Nd and Sr isotopic compositions were determined using a multicollector Finnigan MAT-261 mass spectrometer operated in static multicollector mode at the Isotope Laboratory of the China University of Geosciences, Wuhan. Two aliquots of sample powder (200 mesh), ~100 mg each, were weighed. To one, a known quantity of mixed ^{84}Sr , ^{85}Rb , ^{149}Sm and ^{145}Nd spike solution was added. Samples were digested in Teflon bombs with a mixture of concen-

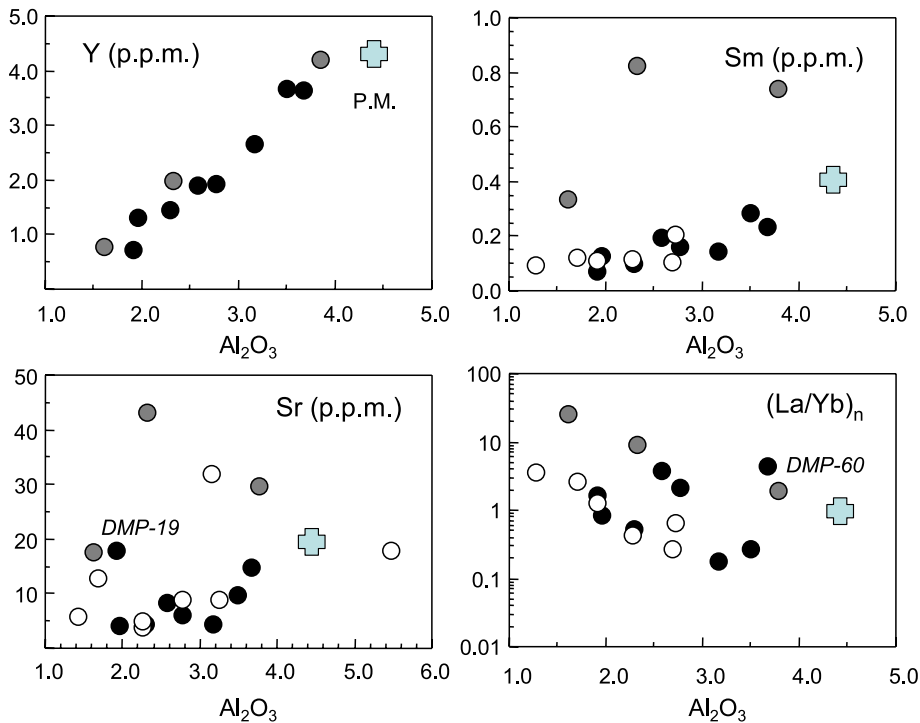


Fig. 6. Moderately incompatible to highly incompatible trace element compositional variations for the Hannuoba xenoliths. ● from this work, ○ from Song and Frey (1989). Gray circles represent the three strongly LREE-enriched peridotites (DMP-23A, DMP-25 and DMP-67C; Fig. 5). Cross denotes primitive mantle (P.M.) from McDonough and Sun (1995). DMP-60, labeled on the $(\text{La}/\text{Yb})_n$ plot (lower right panel), shows a strong increase in La and Ce (see Fig. 5).

trated HF, HNO₃ and HClO₄. The sealed bombs were kept in an oven at 185 °C for 48 h. The decomposed samples were then dried on a hot plate and converted into chlorates by adding more concentrated HClO₄. This was followed by dry down and addition of concentrated HCl to form chlorides, followed by a final evaporation. The dried salts were dissolved again in 500 µl of dilute HCl and then loaded onto columns of AG50W-X8 resin for separation and purification of Rb, Sr and REE, with the REE cut finally loaded on to HDEHP columns for separation of Nd and Sm by HCl eluants. The measured ¹⁴³Nd/¹⁴⁴Nd and ⁸⁷Sr/⁸⁶Sr ratios were normalized to ¹⁴⁶Nd/¹⁴⁴Nd = 0.721900 and ⁸⁶Sr/⁸⁸Sr = 0.11940, respectively. External reproducibility of the isotope measurements can be judged from repeat analyses of international standards. The average ¹⁴³Nd/¹⁴⁴Nd ratio of the La Jolla standard

measured during the sample runs is 0.511862 ± 5 (2σ , $n = 15$). Analysis of BCR-2 gave ¹⁴³Nd/¹⁴⁴Nd = 0.512635 ± 4 , ¹⁴⁷Sm/¹⁴⁴Nd = 0.1369, Nd = 29.10 ppm and Sm = 6.591 ppm, which fall within uncertainty of the recommended values (¹⁴³Nd/¹⁴⁴Nd = 0.512647 ± 22 , 2σ ; White and Patchett, 1984; Nd = 28.8 ppm; Sm = 6.59 ppm; Govindaraju, 1994) for BCR-1. Six analyses of the NBS-987 standard gave ⁸⁷Sr/⁸⁶Sr = 0.710236 ± 16 (2σ , $n = 15$).

5. Petrography

5.1. Hannuoba

The Hannuoba spinel-facies peridotites range from coarse- to medium-grained and have granulite

Table 4
Average EMP analyses of olivines from spinel peridotites

Qixia														
n	Sp lherzolites						Dunite							
	Q1	Q4	Q5	Q6	Q8	Q17	QX-02	QX-07	QX-10	QX-11	QX-13	QX-14	QX-17	QX-18
	5	4	5	6	8	5	5	8	5	8	8	5	5	8
SiO ₂	40.93	40.41	40.76	40.25	40.81	40.33	40.58	41.11	40.60	40.64	41.17	40.28	40.71	41.97
FeO	9.45	9.80	8.82	7.77	8.57	10.23	9.23	9.59	9.75	9.53	9.56	9.25	9.24	1.72
MnO	0.13	0.14	0.12	0.12	0.10	0.15	0.13	0.13	0.14	0.11	0.14	0.14	0.12	0.07
MgO	49.49	48.87	50.03	49.28	48.88	48.92	49.51	49.42	49.24	48.03	49.63	48.98	48.99	54.96
NiO	0.39	0.38	0.41	0.33	0.36	0.37	0.36	0.36	0.35	0.35	0.36	0.36	0.38	0.02
CaO	0.02	0.04	0.03	0.02	0.05	0.02	0.03	0.01	0.03	0.02	0.01	0.02	0.02	0.01
Total	100.41	99.64	100.18	97.76	98.77	100.03	99.85	0.00	100.11	98.68	100.88	99.03	99.45	98.74
Fo	90.3	89.9	91.0	91.9	91.0	89.5	90.5	90.2	90.0	90.0	90.3	90.4	90.4	98.3
Hannuoba														
n	Sp lherzolites													
	DMP04	DMP19	DMP23a	DMP25	DMP41	DMP51	DMP56	DMP58	DMP59	DMP60	DMP67c			
	5	6	6	5	5	4	5	5	5	5	6			
SiO ₂	41.27	41.07	40.85	41.22	40.36	40.49	40.18	40.49	40.60	40.15	40.89			
FeO	8.66	8.38	8.53	8.15	9.34	8.62	9.82	9.42	9.25	9.60	10.10			
MnO	0.12	0.11	0.12	0.10	0.14	0.12	0.15	0.13	0.14	0.14	0.14			
MgO	49.48	49.49	49.01	49.83	49.50	49.21	48.83	48.72	49.01	48.78	48.16			
NiO	0.36	0.37	0.36	0.38	0.39	0.39	0.37	0.37	0.38	0.36	0.35			
CaO	0.03	0.04	0.04	0.06	0.04	0.07	0.06	0.06	0.05	0.05	0.05			
Total	99.91	99.46	98.90	99.75	99.77	98.91	99.39	99.20	99.42	99.07	99.68			
Fo	91.1	91.3	91.1	91.6	90.4	91.1	89.9	90.2	90.4	90.1	89.5			

n: number of individual spot analyses.

Fo: forsterite component = $100 \times \text{molar Mg}/(\text{Mg} + \text{Fe})$.

blastic textures (Fig. 2). Most samples are massive, but a few show foliation defined by aligned spinel grains. In general, both clinopyroxene and orthopyroxenes are homogenous, showing no exsolution lamellae. All xenoliths show alteration along grain boundaries and fractures (typically pale brown serpentine), but the degree of alteration is highly variable from one sample to the next (Fig. 2). A characteristic of the Hannuoba xenoliths is the relative abundance of fresh sulfides, which are found both as inclusions within silicate phases (Fig. 2) or decorating healed fractures.

5.2. Qixia

Qixia spinel-facies peridotites are typically medium-grained with granuloblastic textures. A few sam-

ples are coarse-grained (Q8, QX-09) and/or contain deformed olivine porphyroclasts. Several (QX-11, Q17B) show a pronounced foliation, but most are massive. All show pockets of partially crystallized melt, presumably derived from the host basalt, as the melt pocket abundance increases towards the xenolith margin. Orthopyroxene and clinopyroxene typically contain exsolution lamellae.

6. Results

6.1. Whole rock major and trace element data

Major and trace element analyses of whole rock samples are reported in Table 3 and plotted in Figs. 3–6. Both Hannuoba and Qixia peridotites show a con-

Table 5
Average EMP analyses of orthopyroxene from spinel peridotites

Qixia												
	Q1	Q4	Q5	Q8	Q17	QX-02	QX-07	QX-10	QX-11	QX-13	QX-14	QX-17
<i>n</i>	4	5	4	7	5	8	8	5	8	8	7	3
SiO ₂	56.00	55.71	56.14	56.09	55.32	55.09	55.62	55.39	55.39	55.92	54.83	54.72
TiO ₂	0.07	0.09	0.09	0.01	0.12	0.08	0.08	0.07	0.05	0.08	0.08	0.11
Al ₂ O ₃	3.66	3.81	2.96	2.45	4.06	3.71	4.13	3.57	3.57	3.78	3.46	4.10
Cr ₂ O ₃	0.35	0.19	0.41	0.46	0.25	0.29	0.27	0.27	0.28	0.33	0.23	0.33
FeO	6.32	6.20	5.90	5.54	6.73	6.21	6.28	6.25	5.98	6.30	6.20	6.10
MnO	0.14	0.15	0.12	0.13	0.15	0.15	0.15	0.16	0.14	0.16	0.14	0.13
NiO				0.09			0.09		0.07	0.08		
MgO	34.03	32.26	34.55	33.35	33.19	33.94	33.28	33.86	33.35	33.48	33.60	33.44
CaO	0.47	0.48	0.47	0.55	0.44	0.44	0.39	0.42	0.41	0.39	0.43	0.40
Na ₂ O	0.04	0.05	0.03	0.02	0.05	0.03	0.05	0.06	0.03	0.04	0.04	0.05
Total	101.08	98.93	100.67	98.69	100.29	99.92	100.35	100.05	99.27	100.57	99.01	99.39
Hannuoba												
	DMP-04	DMP-19	DMP-23a	DMP-25	DMP-41	DMP-51	DMP-56	DMP-58	DMP-59	DMP-60	DMP-67c	
<i>n</i>	6	6	9	6	8	7	7	5	9	9	6	
SiO ₂	55.64	55.60	55.63	56.52	55.45	55.47	54.97	55.25	55.29	54.67	54.94	
TiO ₂	0.06	0.03	0.05	0.04	0.07	0.08	0.13	0.09	0.09	0.09	0.13	
Al ₂ O ₃	4.21	3.69	3.84	2.85	3.77	3.67	4.61	4.44	3.95	4.25	5.17	
Cr ₂ O ₃	0.46	0.55	0.50	0.52	0.35	0.46	0.31	0.33	0.41	0.31	0.35	
FeO	5.49	5.15	5.31	5.02	5.90	5.39	6.18	5.94	5.79	6.01	6.26	
MnO	0.12	0.11	0.12	0.11	0.14	0.13	0.12	0.14	0.13	0.13	0.14	
NiO	0.09	0.07	0.08	0.10							0.11	
MgO	33.07	33.39	32.35	33.91	33.87	33.65	32.70	33.08	33.14	33.42	31.96	
CaO	0.64	0.59	0.62	0.61	0.51	0.69	0.70	0.68	0.59	0.56	0.69	
Na ₂ O	0.08	0.07	0.14	0.03	0.08	0.09	0.11	0.12	0.08	0.09	0.14	
Total	99.86	99.24	98.63	99.71	100.14	99.64	99.84	100.08	99.45	99.53	99.89	

n: number of individual spot analyses.

siderable spread in major element compositions, ranging from fertile compositions approaching primitive mantle to refractory harzburgites with up to 45% MgO. These refractory compositions slightly overlap the compositional field of cratonic peridotites, as exemplified by samples from the Tanzanian craton (Rudnick et al., 1994; Lee and Rudnick, 1999) and are distinct from cratonic peridotite averages (Boyd, 1989; Griffin et al., 1999). The Tanzanian xenoliths were chosen as representatives of cratonic lithosphere as they show good correlations on MgO vs. major oxide diagrams (Fig. 3) and do not show the same extent of metasomatic overprinting that some other well-studied cratonic xenoliths exhibit (e.g., Kaapvaal craton samples). In particular, the SiO₂-enrichment that is prevalent in the

Kaapvaal low-temperature peridotites (Boyd, 1989) is rare in the Tanzanian samples (Rudnick et al., 1994; Lee and Rudnick, 1999).

The Qixia samples show more scatter on Al₂O₃ and CaO vs. MgO plots than the Hannuoba xenoliths. This is probably due to their very small sample size and consequently biased mineralogical sampling, and probably also to the presence of the pockets of host basalts described above. For example, sample QX-09 has the highest Al₂O₃ content of the suite and also one of the highest MgO contents, causing it to fall off the negative correlation between Al₂O₃ and MgO (Fig. 3). However, this sample is anomalous in no other way and plots within the data array on the CaO, FeO and SiO₂ vs. MgO diagrams and has mineral compositions

Table 6
Average EMP analyses of clinopyroxenes from spinel peridotites

Qixia													
	Q1	Q4	Q5	Q6	Q8	Q17	QX-02	QX-07	QX-10	QX-11	QX-13	QX-14	QX-17
<i>n</i>	5	5	5	7	6	5	7	7	7	7	8	7	5
SiO ₂	52.57	52.68	52.53	54.44	53.72	52.08	52.42	52.51	52.36	52.20	52.68	51.32	51.35
TiO ₂	0.31	0.50	0.36	0.03	0.03	0.62	0.42	0.50	0.39	0.43	0.46	0.43	0.55
Al ₂ O ₃	5.46	6.87	4.58	1.90	2.62	7.16	5.84	7.14	6.46	6.20	6.38	6.14	6.45
Cr ₂ O ₃	0.77	0.72	1.21	0.77	0.84	0.70	0.73	0.80	0.76	0.77	0.91	0.69	0.71
FeO	2.45	2.43	2.15	1.92	2.14	2.62	2.27	2.32	2.23	2.39	2.43	2.40	2.35
MnO	0.08	0.08	0.07	0.07	0.08	0.09	0.08	0.07	0.09	0.07	0.08	0.07	0.09
MgO	15.31	14.57	15.66	17.26	17.11	14.21	15.16	14.32	14.83	14.66	14.76	14.86	14.56
CaO	21.49	20.74	21.67	22.95	22.69	20.58	21.49	20.49	21.02	21.26	21.12	21.31	20.61
Na ₂ O	1.49	1.94	1.45	0.47	0.31	2.15	1.55	1.87	1.54	1.53	1.60	1.43	1.94
Total	99.93	100.51	99.69	99.80	99.54	100.21	99.96	100.03	99.67	99.50	100.42	98.66	98.61
Mg#	91.8	91.5	92.9	94.1	93.4	90.6	92.3	91.7	92.2	91.6	91.6	91.7	91.7
Hannuoba													
	DMP-04	DMP-19	DMP-23a	DMP-25	DMP-41	DMP-51	DMP-56	DMP-58	DMP-59	DMP-60	DMP-67c		
<i>n</i>	7	6	5	7	9	5	8	9	10	10	7		
SiO ₂	53.00	52.88	52.73	53.41	52.56	52.81	52.23	52.54	52.51	52.08	51.31		
TiO ₂	0.26	0.14	0.13	0.13	0.35	0.27	0.60	0.38	0.39	0.45	0.92		
Al ₂ O ₃	5.66	5.02	3.25	3.49	6.13	4.96	6.62	6.32	5.65	6.49	4.56		
Cr ₂ O ₃	0.92	1.28	1.24	1.09	0.99	0.96	0.66	0.73	0.91	0.75	0.85		
FeO	2.35	1.96	2.45	2.03	2.26	2.33	2.79	2.66	2.33	2.33	3.43		
MnO	0.08	0.08	0.09	0.08	0.08	0.07	0.08	0.09	0.08	0.09	0.11		
MgO	15.71	15.67	16.66	16.75	15.30	16.10	15.23	15.51	15.44	15.23	16.19		
CaO	20.26	20.46	21.33	21.25	20.58	20.35	19.61	19.79	20.62	20.06	21.10		
Na ₂ O	1.35	1.31	0.51	0.79	1.77	1.35	1.73	1.72	1.57	1.71	0.46		
Total	99.58	98.82	98.39	99.00	100.03	99.21	99.54	99.74	99.50	99.19	98.93		
Mg#	92.3	93.4	92.4	93.6	92.3	92.5	90.7	91.2	92.2	92.1	89.4		

n: number of individual spot analyses.

Mg# = 100 × molar Mg/(Mg + Fe).

similar to other samples (Tables 4–7; Fig. 7). The high Al₂O₃ content may reflect an oversampling of spinel in the whole rock powder. Similar sampling biases may explain the two samples from the literature that fall below the Al₂O₃–MgO array (Fig. 3)—in this case, an undersampling of spinel. For these reasons, the mineral chemical data for Qixia xenoliths are viewed as a more reliable indication of rock composition than the whole rock data.

Compatible (Ni) and moderately incompatible (V, Cu, Y) trace elements show positive and negative correlations, respectively, when plotted against MgO

(Fig. 4). In contrast, highly incompatible trace elements (La, Ce, Nb, Ta, Ba, Sr, Th, U) show no correlation with MgO and are only poorly correlated with each other (not shown). As for the major elements, the compatible and moderately incompatible trace element abundances of these Chinese samples are distinct from those of cratonic peridotites (Fig. 4).

Rare earth element (REE) patterns of the Hannuoba spinel-facies peridotites are plotted in Fig. 5. The patterns range dramatically from light REE (LREE) depleted to LREE-enriched, with a number of samples having flat and U-shaped REE patterns. A comparison

Table 7
Average EMP analyses of spinel from spinel peridotites

		Qixia												
		Q1	Q4	Q5	Q6	Q8	Q17	QX-02	QX-07	QX-10	QX-11	QX-13	QX-14	QX-17
<i>n</i>		5	5	5	9	6	5	5	4	5	6	6	5	5
TiO ₂		0.05	0.05	0.12			0.06	0.05		0.05			0.04	0.06
V ₂ O ₅		0.09	0.07	0.15			0.05	0.07		0.07			0.08	0.05
Al ₂ O ₃		56.44	60.07	45.79	29.01	35.94	60.72	58.83	59.22	59.05	59.22	56.20	58.63	59.43
Cr ₂ O ₃		11.81	8.54	22.50	39.67	32.48	8.01	10.38	9.45	10.00	9.84	12.23	8.84	9.10
FeO		11.64	10.41	12.94	16.58	14.36	11.26	10.38	10.62	10.76	10.45	11.58	10.78	10.49
MnO		0.10	0.09	0.12	0.19	0.13	0.11	0.10	0.07	0.08	0.08	0.10	0.09	0.09
MgO		19.99	20.52	18.55	15.31	17.63	20.50	20.54	21.37	20.24	21.46	20.82	20.45	20.43
NiO		0.36	0.40	0.28			0.40	0.32		0.36			0.37	0.35
ZnO		0.09	0.08	0.13			0.08	0.10		0.10			0.09	0.09
Total		100.56	100.23	100.57	100.75	100.53	101.19	100.77	100.72	100.70	101.05	100.92	99.38	100.10
Cr#		12.3	8.7	24.8	47.9	37.8	8.1	10.6	9.7	10.2	10.0	12.7	9.2	9.3
Mg#		75.4	77.8	71.9	62.2	68.6	76.5	77.9	78.2	77.0	78.5	76.2	77.2	77.6
		Hannuoba												
		DMP-04	DMP-19	DMP-23a	DMP-25	DMP-41	DMP-51	DMP-56	DMP-58	DMP-59	DMP-60	DMP-67c		
<i>n</i>		6	5	5	5	5	6	5	5	5	5	6		
TiO ₂						0.09	0.14	0.16	0.11	0.11	0.10			
V ₂ O ₅						0.07	0.11	0.06	0.08	0.08	0.07			
Al ₂ O ₃		52.87	46.35	43.89	37.39	57.09	49.32	58.66	57.36	54.85	59.11	57.34		
Cr ₂ O ₃		15.90	22.39	24.33	31.33	12.49	18.65	8.76	10.39	13.33	9.00	9.43		
FeO		10.34	10.21	11.94	11.72	10.12	10.65	10.23	10.19	10.15	9.60	12.84		
MnO		0.10	0.09	0.11	0.13	0.09	0.10	0.09	0.09	0.10	0.09	0.09		
MgO		21.20	20.14	19.39	18.85	20.50	19.68	21.05	20.94	20.36	20.84	20.63		
NiO						0.34	0.30	0.40	0.34	0.33	0.40			
ZnO						0.06	0.06	0.05	0.06	0.06	0.07			
Total		100.41	99.18	99.66	99.41	100.85	99.02	99.46	99.56	99.36	99.26	100.33		
Cr#		16.8	24.5	27.1	36.0	12.8	20.2	9.1	10.8	14.0	9.3	9.9		
Mg#		78.5	77.9	74.3	74.1	78.3	76.7	78.6	78.6	78.1	79.5	74.1		

n: number of individual spot analyses.

Cr# = 100 × molar Cr/(Cr + Al).

Mg# = 100 × molar Mg/(Mg + Fe).

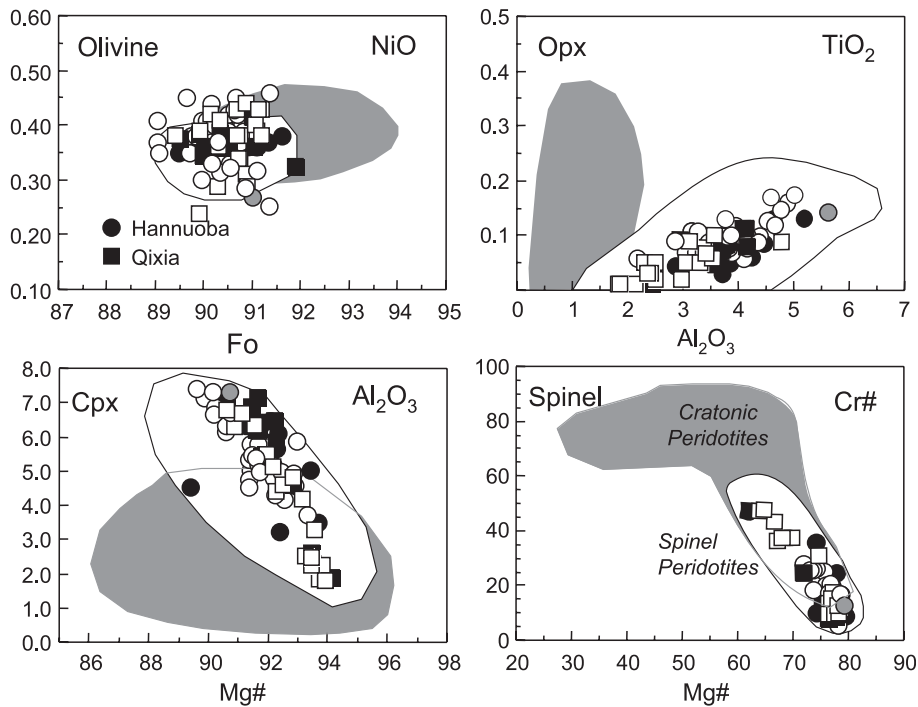


Fig. 7. Mineral compositional plots for Hannuoba and Qixia spinel peridotites and a single garnet lherzolite from Hannuoba (HT-28 from Fan and Hooper, 1989). Circles are data for Hannuoba spinel peridotites: \circ are previously published data (Fan and Hooper, 1989; Song and Frey, 1989; Chen et al., 2001); \bullet are data from this study; the gray circle is garnet peridotite HT-28. \blacksquare are data from Qixia xenoliths (this study) and \square are previously published data (Fan and Hooper, 1989; Zheng et al., 1998). OPX: orthopyroxene; CPX: clinopyroxene. Open field is for worldwide spinel peridotites and gray field encompasses minerals from cratonic peridotites (including Kaapvaal, east Greenland, Siberia and Tanzania).

between clinopyroxene REE patterns and whole rock patterns by Song and Frey (1989) showed that whole rocks consistently have higher La/Sm than the clinopyroxene, indicating that some LREE reside elsewhere in the peridotite (e.g., on grain boundaries or in accessory phases). Furthermore, mass balance calculations, described below, show that two of the samples investigated here (DMP-41 and DMP-59) contain a significant amount of LREE in phases other than clinopyroxene. Both these samples have U-shaped REE patterns and relatively high concentrations. The origin of the LREE mass balance discrepancies is considered further in the Discussion. These differences notwithstanding, Song and Frey (1989) generally found that clinopyroxene and whole rock REE patterns are quite similar, especially for the middle to heavy REE (HREE), implying that the whole rock REE pattern faithfully records the pre-entrainment REE pattern of the peridotite. This conclusion is supported by LA-ICP-MS clinopyroxene analyses (Gao et al.,

unpublished data), which generally mimic the whole rock REE pattern, including the unusual LREE enrichment seen in sample DMP-60 (Fig. 5). Clinopyroxenes from this sample and DMP-59 show zoned La and Ce concentrations, with marked La and Ce enrichment on the mineral rims (Pr and heavier REE do not vary from rim to core). Other incompatible trace elements (e.g., Rb, Sr, Ba) also showed enrichments on the rims. No other clinopyroxenes were observed to exhibit REE zoning in this study, but Song and Frey (1989) describe one of their samples as also having compositionally heterogeneous clinopyroxene (DM1–3). This sample also has a U-shaped REE pattern.

Excellent correlations are observed for Y vs. Al_2O_3 (Fig. 6), which are similar to those observed globally in anhydrous peridotites (McDonough and Frey, 1989). The HREE show similar correlations (not shown). The middle REE (Sm to Gd) also show positive correlations when plotted against Al_2O_3 , except that samples with the greatest LREE enrichments (the LREE enriched

Table 8
Modal mineralogy^a of Hannuoba peridotites

	Ol	Opx	Cpx	Sp	Total	SSQ ^b
DMP-04	67.5	21.9	8.9	1.6	99.9	0.0
DMP-19	61.7	29.8	7.8	0.8	100.0	0.1
DMP-23a	64.5	27.1	6.3	2.0	100.0	0.5
DMP-25	70.3	24.2	3.8	1.5	99.8	0.2
DMP-41	57.5	30.9	9.6	1.9	99.8	0.1
DMP-51	64.4	27.0	7.6	0.9	100.0	0.1
DMP-56	54.9	27.7	15.3	2.1	100.0	0.1
DMP-58	56.7	28.4	13.0	2.0	100.0	0.2
DMP-59	63.5	23.6	11.0	1.9	100.0	0.2
DMP-60	44.7	37.4	16.1	1.8	100.0	0.2
DMP-67c	55.7	27.8	12.9	3.2	99.6	0.2

Ol: olivine; Opx: orthopyroxene; Cpx: clinopyroxene; Sp: spinel.

^a Calculated using MINSQ (Hermann and Berry, 2002). See text for details.

^b Sum of squared residuals.

samples in Fig. 5) fall off the trend defined by the other samples. In contrast, there is no correlation between LREE concentrations and Al₂O₃ (not shown), or between the most highly incompatible trace elements and any other elements or equilibration temperature. There is a weak, negative correlation between the degree of LREE enrichment [as reflected by (La/Yb)_n] and Al₂O₃, with the data for our samples showing considerably more scatter than those of Song and Frey (1989), and the most LREE-enriched samples falling off the trend established by the others.

6.2. Mineral chemistry, modes and thermometry

Mineral chemical data are reported in Tables 4–7 and plotted in Fig. 7. Minerals in these xenoliths are homogenous (based on several core and rim analyses in each sample), and thus, average compositions are reported. Mineral compositions of Qixia and Hannuoba peridotites overlap significantly, although it appears that Qixia samples range to slightly more refractory compositions than the Hannuoba samples, based on the Cr# of spinels (Fig. 7). The minerals in the Chinese xenoliths are identical to those of off-craton spinel peridotite xenoliths, worldwide, but are clearly distinct from those in cratonic peridotites (Fig. 7). Although the general absence of garnet in the Chinese samples will result in higher Al₂O₃ contents in pyroxenes and spinels (hence, lower Cr# in the latter) compared with garnet-bearing cratonic peridotites, it is interesting to note that the single

garnet-bearing, refractory (Fo₉₁) spinel lherzolite from Hannuoba (sample HT-28 of Fan and Hooper, 1989) contains pyroxenes with high Al₂O₃ and TiO₂ contents and spinels with low Cr# and falls within the spinel-facies peridotite data arrays in Fig. 7. Therefore, these mineral compositional differences between cratonic peridotites and the North China craton samples primarily reflect differences in bulk rock compositions, rather than differences in facies (garnet vs. spinel) or temperature, and high-

Table 9
Equilibration temperatures (°C) of spinel lherzolite and pyroxenite xenoliths, calculated from average mineral compositions

Sample	T Ca in Opx	T _{BKN}	Wells	N&T
<i>Qixia</i>				
Q1	880	850	860	785
Q4	890	880	875	790
Q5	880	815	840	750
Q6				920
Q8	920	950	970	955
Q17	870	820	825	720
QX-02	870	835	850	765
QX-07	850	925	895	840
QX-09	915	950	895	865
QX-10	860	910	890	840
QX-11	860	865	865	790
QX-13	847	902	888	830
QX-14	870	840	850	770
QX-17	855	810	825	720
<i>Hannuoba</i>				
DMP-04	950	1050	1005	990
DMP-19	930	1020	985	965
DMP-23a	945	1035	1035	990
DMP-25	940	1030	1010	990
DMP-41	900	935	910	990
DMP-51	965	1030	990	990
DMP-56	970	1040	985	980
DMP-56px	960	1020	965	980
DMP-58	960	1030	980	985
DMP-59	930	1000	960	990
DMP-60	920	990	945	990
DMP-67c	965	1055	1040	960
JSB-01px	960	1015	965	980

Temperatures are rounded to nearest 5 °C.

T Ca in Opx: calcium in opx thermometer of Brey and Köhler (1990).

T_{BKN}: opx–cpx thermometer of Brey and Köhler (1990).

Wells: two-pyroxene thermometer of Wells (1977).

N&T: cpx thermometer of Nimis and Taylor (2000).

Pressure of 1.5 GPa assumed throughout.

“px”: pyroxenite.

light further the noncratonic character of the Hannuoba and Qixia peridotites.

Modal mineralogy, calculated from least squares mixing of mineral proportions to match whole rock compositions, is presented in Table 8 for the Hannuoba samples. The calculations were performed using the MINSQ program of Hermann and Berry (2002). All whole rock analyses used in the calculation were summed to 100% anhydrous and all Fe is reported as FeO. Hermann and Berry suggested that a value of the sum of squared residuals (SSQ) of less than 0.5 is an acceptable outcome in most cases. All of the modes shown in Table 8 conform to this criterion. Similar calculations were not performed for the Qixia xenoliths because the overall small sample sizes makes the validity of any modes calculated from whole rock data uncertain.

Equilibration temperatures calculated from selected cation exchange thermometers are given in Table 9 and are plotted in Figs. 8 and 9. Several features are

apparent from these diagrams. Firstly, although there is a positive correlation between temperatures calculated from different thermometers, the degree of correlation between different thermometers is variable. For example, Ca-in-orthopyroxene temperatures (Brey and Köhler, 1990) show considerable scatter when plotted against two-pyroxene temperatures for both the Hannuoba and Qixia data sets (Fig. 8, upper panels). In contrast, the Wells (1977) and Brey and Köhler (1990) calibrations of the two-pyroxene thermometer show a tighter correlation (Fig. 8, lower panels), with Hannuoba data falling within a fairly narrow array and Qixia data showing more scatter. Similar correlations are observed between temperatures calculated using the Nimis and Taylor (2000) clinopyroxene thermometer and the two-pyroxene temperatures (not shown).

Secondly, there appears to be a systematic offset in temperatures calculated using data from different laboratories for all but the lower left panel in Fig. 8. The

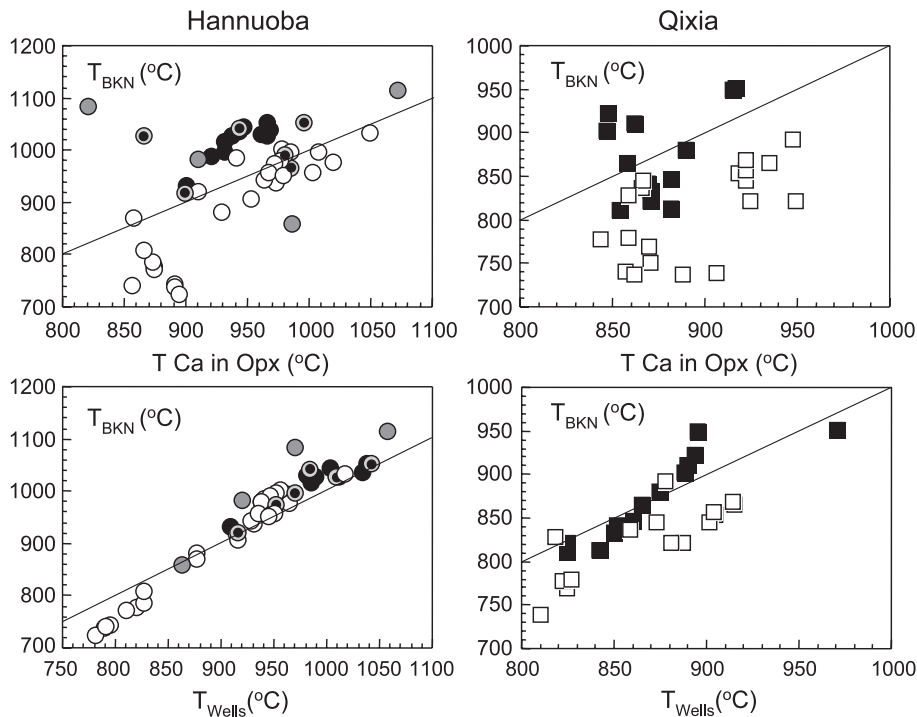


Fig. 8. Comparison of equilibration temperatures calculated from Ca-in-orthopyroxene (Brey and Köhler, 1990) and two-pyroxene thermometers given by Wells (1977) and Brey and Köhler (1990) (BKN) for Hannuoba (circles) and Qixia (squares) peridotite xenoliths. Filled symbols are temperatures calculated from data in Table 9 (this study); open symbols are calculated from the published data of Chen et al. (2001) for Hannuoba, and Zheng et al. (1998) for Qixia. Gray circles are calculated from data of Fan and Hooper (1989) and gray circles with black centers are calculated from data of Song and Frey (1989).

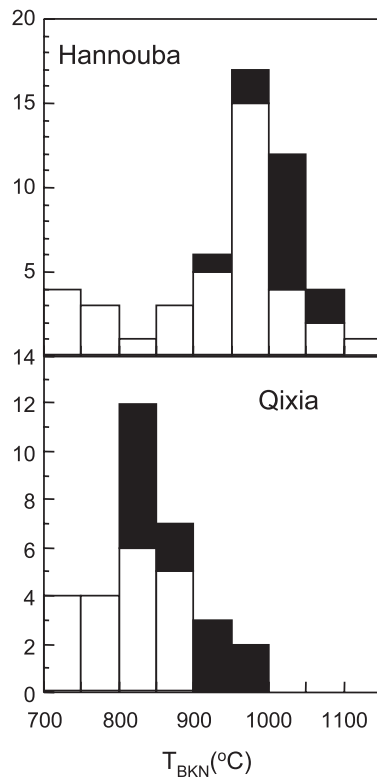


Fig. 9. Two pyroxene equilibration temperature histogram for Hannuoba (upper) and Qixia (lower) spinel peridotite xenoliths. Temperatures calculated using the Brey and Köhler (1990) calibration. Filled symbols are temperatures calculated from data in Table 9 (this study); open symbols are calculated from the published data of Song and Frey (1989), Fan and Hooper (1989) and Chen et al. (2001) for Hannuoba, and Zheng et al. (1998) for Qixia.

open symbols in Fig. 8 were calculated from microprobe data gathered at Macquarie University (Zheng et al., 1998; Chen et al., 2001), and these temperatures are systematically offset from those calculated from the data presented here, which were gathered at Harvard University and the University of Maryland. The published data of Song and Frey (1989) scatter between the two data sets in the upper panels but follow the good correlation in the lower panels, whereas results from the published data of Fan and Hooper (1989—gray circles) scatter the most of any data set. It is likely that the offset in temperatures reflects EMP calibration differences for Ca in orthopyroxene between different labs, highlighting the sensitivity of this thermometer to small differences in calibration. Because of this scatter,

we will use only two pyroxene temperatures in further discussion of equilibration temperatures.

Finally, there appears to be a real temperature difference between the Hannuoba and Qixia xenoliths. The Hannuoba data set shows a large range in equilibration temperatures, from 725 to 1100 °C, whereas the Qixia temperatures are generally <900 °C (Fig. 9). In addition, there is no correlation between equilibration temperature and major element, trace element or isotopic composition for either xenolith suite, indicating that the lithospheric mantle is not compositionally stratified beneath these two areas of the North China craton.

6.3. Sr and Nd isotopes

The Sr and Nd isotopic compositions of both whole rocks and clinopyroxene separates from the Hannuoba xenoliths are given in Table 10 and plotted in Figs. 10–12 along with previously published data for both Hannuoba (Song and Frey, 1989; Fan et al., 2000) and Qixia (Fan et al., 2000). Two of the clinopyroxene separates have been run in duplicate. For one of these (DMP-58 cpx), the $^{143}\text{Nd}/^{144}\text{Nd}$ reproduces within uncertainty, but not the $^{87}\text{Sr}/^{86}\text{Sr}$, which is quite different between the two duplicates. For the other (DMP-60 cpx), $^{87}\text{Sr}/^{86}\text{Sr}$ is reproduced within uncertainty but $^{143}\text{Nd}/^{144}\text{Nd}$ is not. This irreproducibility of Nd in clinopyroxene from DMP-60 is consistent with the zoning in LREE, as revealed by LA-ICP-MS analyses (Gao et al., unpublished data) and the unusual whole rock REE pattern (Fig. 5), and suggests that the zoning may be accompanied by isotopic variations (cf. Schmidberger et al., 2003, who found Sr isotope heterogeneities within single clinopyroxenes from peridotites from Somerset Island). The only other sample that shows similar zoning of LREE in clinopyroxene is DMP-59, which is also characterized by extreme enrichments of LREE on the rims.

The whole rock Nd and Sr isotopic compositions generally do not match those of the clinopyroxenes (Fig. 10). In most cases, the whole rocks have more radiogenic $^{87}\text{Sr}/^{86}\text{Sr}$ and/or less radiogenic $^{143}\text{Nd}/^{144}\text{Nd}$ compared to the clinopyroxene. However, one sample (DMP-19) has clinopyroxene with *less* radiogenic Nd than the whole rock, and another sample (DMP-41) has clinopyroxene with *more* radiogenic Sr than the whole rock. Table 11 shows mass balances for

Table 10
Sr and Nd isotopic data for whole rock and Cr-diopside separates from Hannuoba peridotites

		Nd (ppm)	Sm (ppm)	$^{147}\text{Sm}/$ ^{144}Nd	$^{143}\text{Nd}/$ ^{144}Nd	$\pm 2\sigma$	ϵ_{Nd}	Sr (ppm)	Rb (ppm)	$^{87}\text{Rb}/^{86}\text{Sr}$	$^{87}\text{Sr}/^{86}\text{Sr}$	$\pm 2\sigma$
DMP-04	Whole rock	0.22	0.08	0.2183	0.513185	40	10.7	4.51	0.26	0.1685	0.704442	61
DMP-04-cpx	Cr diopside	2.82	0.99	0.2122	0.513143	8	9.9	39.6	0.58	0.0426	0.703634	20
DMP-05-cpx	Cr diopside	4.95	1.83	0.2230	0.513165	8	10.3	66.8	0.17	0.0074	0.703026	18
DMP-19	Whole rock	0.25	0.06	0.1554	0.513068	25	8.4	18.8	0.74	0.1138	0.704369	24
DMP-19-cpx	Cr diopside	3.28	0.97	0.1781	0.512832	8	3.8	76.4	0.24	0.0090	0.704353	21
DMP-23a	Whole rock	3.24	0.75	0.1392	0.513033	16	7.7	47.6	1.97	0.1195	0.703709	17
DMP-25	Whole rock	1.78	0.33	0.1139	0.512921	8	5.5	20.4	2.09	0.2965	0.704585	19
DMP-41	Whole rock	0.62	0.19	0.1885	0.513025	13	7.5	6.63	0.14	0.0632	0.703396	40
DMP-41-cpx	Cr diopside	3.10	1.16	0.2269	0.513359	9	14.1	57.8	0.21	0.0105	0.703696	22
DMP-51	Whole rock	0.2	0.08	0.2387	0.513280	22	12.5	3.64	0.32	0.2558	0.703889	55
DMP-56	Whole rock	0.65	0.26	0.2409	0.513294	10	12.8	10.8	0.34	0.0920	0.703337	75
DMP-56-cpx	Cr diopside	4.32	1.74	0.2428	0.513241	7	11.8	65.1	0.30	0.0132	0.702571	19
DMP-58	Whole rock	0.23	0.13	0.3395	0.513149	25	10.0	5.05	0.49	0.2789	0.704485	60
DMP-58-cpx	Cr diopside	1.45	0.99	0.4132	0.513645	10	19.6	27.3	0.16	0.0166	0.703246	29
DMP-58-cpx duplicate	Cr diopside	1.45	1.00	0.4161	0.513651	10	19.8	27.3	0.16	0.0173	0.703759	38
DMP-59	Whole rock	0.8	0.17	0.1269	0.513127	11	9.5	8.96	0.43	0.1395	0.704515	32
DMP-59-cpx	Cr diopside	2.96	1.00	0.2047	0.513327	8	13.4	69.4	0.51	0.0214	0.703717	18
DMP-60	Whole rock	0.46	0.21	0.2759	0.513154	78	10.1	16.3	0.29	0.0515	0.703232	18
DMP-60-cpx	Cr diopside	2.74	1.21	0.2669	0.513831	16	23.3	154	0.29	0.0055	0.703252	18
DMP-60-cpx duplicate	Cr diopside	3.00	1.35	0.2719	0.513780	15	22.3	155	0.31	0.0058	0.703153	29
DMP-67c	Whole rock	2.38	0.64	0.1642	0.512963	9	6.3	32.4	4.11	0.3670	0.705446	17

Nd and Sr based on the measured clinopyroxene and whole rock concentrations and the modal clinopyroxene calculations from Table 8. Because the latter are estimated to have uncertainties on the order of $\pm 10\%$, only mass balance discrepancies greater than 10% are considered significant. As can be seen from the table, all but one sample show significantly more Sr in the whole rock than can be accounted for by the clinopyroxene alone, and several samples also show significantly more Nd in the whole rock than can be accounted for by the clinopyroxene. Indeed, one sample (DMP-59) has one and one-half times more Nd in the whole rock than is present in the clinopyroxene. This sample has an elevated, U-shaped REE pattern and has clinopyroxene that is strongly zoned in LREE. The significance of these differences between clinopyroxene and whole rock Sr and Nd compositions are returned to in the Discussion.

Our Hannuoba clinopyroxene data range to higher $^{143}\text{Nd}/^{144}\text{Nd}$ than previously published data, and generally have higher $^{87}\text{Sr}/^{86}\text{Sr}$ for a given $^{143}\text{Nd}/^{144}\text{Nd}$ (Fig. 11). The latter may reflect a labile Sr component in the unleached clinopyroxenes analysed here. The

clinopyroxene data form a positive trend on a Sm–Nd isochron diagram (Fig. 12) but do not show any correlation on a Rb–Sr isochron diagram (not shown). The clinopyroxene Nd and Sr data (both published and our new results) correlate with major element compositions (as noted by Song and Frey), with more fertile compositions having higher $^{143}\text{Nd}/^{144}\text{Nd}$ and lower $^{87}\text{Sr}/^{86}\text{Sr}$ (Fig. 13). As for the Sr–Nd isotope plot (Fig. 11), our $^{87}\text{Sr}/^{86}\text{Sr}$ data are offset to higher values than published data (Fig. 13).

7. Discussion

7.1. Origin of the peridotites and major element systematics

The major element, compatible and moderately incompatible trace element and mineral chemical data for the Hannuoba and Qixia spinel peridotite xenoliths reflect their origin as residues from variable degrees of partial melting of a primitive mantle composition (Figs. 3, 4, 7). Based on major element systematics

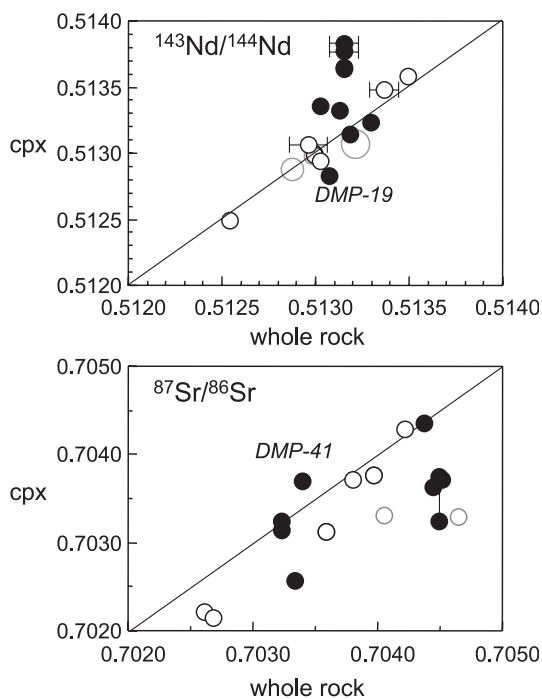


Fig. 10. Comparison of Nd and Sr isotopic compositions of clinopyroxenes and whole rocks for Hannuoba peridotites. Analytical uncertainties (2σ) are generally equal to or smaller than the symbol size, except where shown. Filled circles are data from Table 10; open black circles are data from Song and Frey (1989) and open gray circles are data from Tatsumoto et al. (1992). Diagonal line marks condition of whole rock = clinopyroxene. Only a few whole rocks have isotopic compositions within uncertainty of the clinopyroxene values. Most whole rocks have elevated $^{87}\text{Sr}/^{86}\text{Sr}$ and lower $^{143}\text{Nd}/^{144}\text{Nd}$ than the clinopyroxene separates.

(Fig. 3; Table 3) and published experimental melting studies, these peridotites may reflect between 0% to 25% removal of a batch melt from a primitive mantle composition at pressures between 1 and 3 GPa (Walter, 1999). The lack of correlation between equilibration temperature and major element composition in either suite shows that the lithosphere is not chemically stratified beneath the North China craton. Thus, variations in degree of partial melting are not easily related to a simple lithospheric column generated during a single upwelling event, where shallower residues are predicted to be more refractory than deeper residues.

These same geochemical parameters also demonstrate that both lithospheric sections overlap substantially in terms of their bulk composition, although the

partial melting events in which they formed were widely separated in time (by >1300 Ma; Gao et al., 2002). There is thus no indication in these data that Phanerozoic lithosphere is any less refractory than Proterozoic lithosphere (Griffin et al., 1999; O'Reilly et al., 2001). Indeed, on average, the Mesozoic lithosphere studied may be slightly more refractory than Proterozoic lithosphere, based on spinel compositions that range to slightly higher Cr# in the Qixia samples (Fig. 7).

Another important observation from these data is that both lithospheric sections are compositionally distinct from the highly refractory mantle lithosphere that characterizes Archean cratons (Figs. 3, 4, 7). This is consistent with previous observations from the North China craton (Menzies et al., 1993; Griffin et al., 1998; Zheng et al., 1998; Fan et al., 2000) and, coupled with Os isotope results (Gao et al., 2002), documents replacement of cratonic lithosphere that occurred in two separate episodes: (1) the Proterozoic, beneath the Central Orogenic Belt and (2) the Mesozoic, beneath the Eastern Block (Fig. 1).

7.2. Sr and Nd variations between clinopyroxene and whole rocks

Discrepancies in Nd and Sr mass balance and differences in Nd and especially Sr isotopic compositions between whole rocks and clinopyroxenes in the Hannuoba peridotites may reflect one or both of the following: (1) addition of Sr and/or Nd on grain boundaries during metasomatism, host basalt infiltration or posteruption alteration; (2) the presence of Sr- or Nd-bearing accessory phases that may or may not be in isotopic equilibrium with the clinopyroxene.

Whole rocks with higher $^{87}\text{Sr}/^{86}\text{Sr}$ and/or lower $^{143}\text{Nd}/^{144}\text{Nd}$ than their paired clinopyroxene may be explained by a grain boundary phase (glass or alteration) that is isotopically more evolved than the clinopyroxene (e.g., Zindler and Jagoutz, 1988). Such an explanation can account for most of the whole rock–clinopyroxene Sr isotope differences observed here. In all but one sample (DMP-56), the whole rock Sr abundance is significantly (i.e., >10%) greater than that accounted for by the clinopyroxene. However, not all samples with elevated Sr contents have radiogenic whole rock compositions. In fact, the samples with the largest mass balance discrepancies for Sr (DMP-19

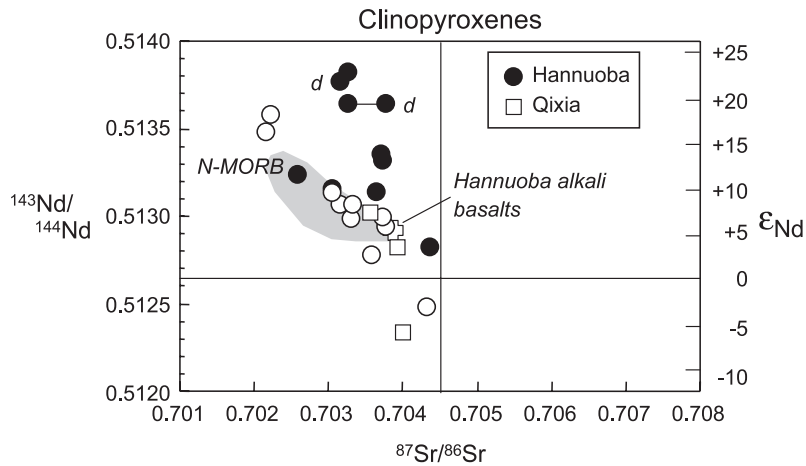


Fig. 11. Nd and Sr isotopic compositions of clinopyroxenes from Hannuoba and Qixia spinel peridotites. Duplicate analyses are connected by tielines or labeled with “d”. Filled circles are data from this study. Open circles are previously published data from Song and Frey (1989), Tatsumoto et al. (1992) and Fan et al. (2000). Qixia data (squares) are from Fan et al. (2000). Open cross represents range in isotopic composition of Hannuoba alkali basalts (from Song et al., 1990). Field of N-MORB is from PetDB (Lehnert et al., 2000) for Atlantic and Pacific MORB.

and DMP-60, for which 70–85% of the whole rock Sr is *not* in clinopyroxene; Table 11) do not exhibit differences in the Sr isotopic compositions between clinopyroxene and host rock. This suggests one of two

possibilities. Firstly, the “missing” Sr may occur in a Sr-rich accessory phase that is in isotopic equilibrium with the clinopyroxene. However, we are at a loss to identify this phase from either thin section or bulk rock

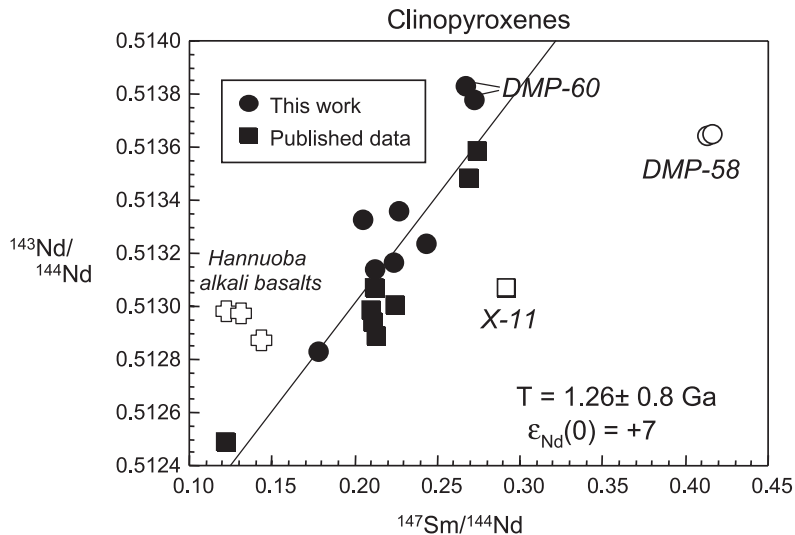


Fig. 12. Sm–Nd isochron plot for Hannuoba clinopyroxene separates from this study (circles) and previously published data (squares) from Song and Frey (1989) and Tatsumoto et al. (1992). Open crosses represent compositions of Damaping basalts that are the hosts to the xenoliths ($^{143}\text{Nd}/^{144}\text{Nd}$ data from Song et al., 1990; $^{147}\text{Sm}/^{144}\text{Nd}$ calculated from Sm and Nd data in Zhi et al., 1990). Linear regression yields “errorchron” of ca. 1.3 Ga with a high initial ϵ_{Nd} of +7. Samples plotted as labeled open symbols were not included in the regression.

Table 11
Mass balance of Sr and Nd in Hannuoba peridotites

Sample	Cpx mode (%)	Sr wr meas. (ppm)	Sr wr calc. (ppm)	Difference (meas. – calc.)	Percentage of difference (%)	Nd wr meas. (ppm)	Nd wr calc. (ppm)	Difference (meas. – calc.)	Percentage of difference (%)
DMP-04	8.9	4.51	3.53	1.0	22	0.22	0.25	–0.03	–12
DMP-19	7.8	18.8	5.96	12.8	68	0.25	0.26	–0.01	–2
DMP-41	9.6	6.63	5.55	1.1	16	0.62	0.30	0.32	108
DMP-56	15.3	10.83	9.96	0.9	8	0.65	0.66	–0.01	–2
DMP-58	13.0	5.05	3.54	1.5	30	0.23	0.19	0.04	22
DMP-59	11.0	8.96	7.63	1.3	15	0.80	0.33	0.47	146
DMP-60	16.1	16.3	2.62	13.7	84	0.46	0.44	0.02	4

chemistry. For example, neither of these samples have particularly high P_2O_5 , which suggests that apatite is not the culprit. Alternatively, the Sr may occur in Sr-

rich grain boundary melts that have equilibrated with the clinopyroxene in some, but not all, xenoliths prior to their entrainment in the host basalt. One of the samples with “missing” Sr (DMP-60) also has clinopyroxenes that are zoned with respect to Sr and the LREE, and shows the greatest discrepancy in Nd isotopic composition between clinopyroxene and whole rock (the clinopyroxene is 10 ϵ units lower than the whole rock). Infusion of a LILE-enriched melt from an isotopically evolved source, coupled with faster Sr diffusion and isotopic equilibration compared to LREE (Sneeringer et al., 1984; Van Orman et al., 2001) may therefore explain these observations. However, this scenario does not explain why Nd mass balances in this sample. That is, all of the Nd appears to be accounted for by the zoned clinopyroxene.

A radiogenic, Sr-rich grain boundary phase is consistent with the results of Song and Frey (1989) who found leached clinopyroxenes to yield generally lower $^{87}Sr/^{86}Sr$ than the whole rocks and the leachates to have higher $^{87}Sr/^{86}Sr$ than the whole rocks. However, one of our samples (DMP-41) has a whole rock composition that is less radiogenic than the clinopyroxene, which accounts for only 84% of the total Sr. This result suggests either the presence of an additional Sr-bearing phase that is less radiogenic than the clinopyroxene (0.7037), or the presence of isotopically zoned clinopyroxene, which may have formed during recent metasomatic overprinting (e.g., Schmidberger et al., 2003).

The correspondence between the Nd isotopic composition of clinopyroxenes and whole rocks is generally much better than for Sr (Fig. 10) and where discrepancies do exist, the clinopyroxene is generally more radiogenic than the whole rock, consistent with

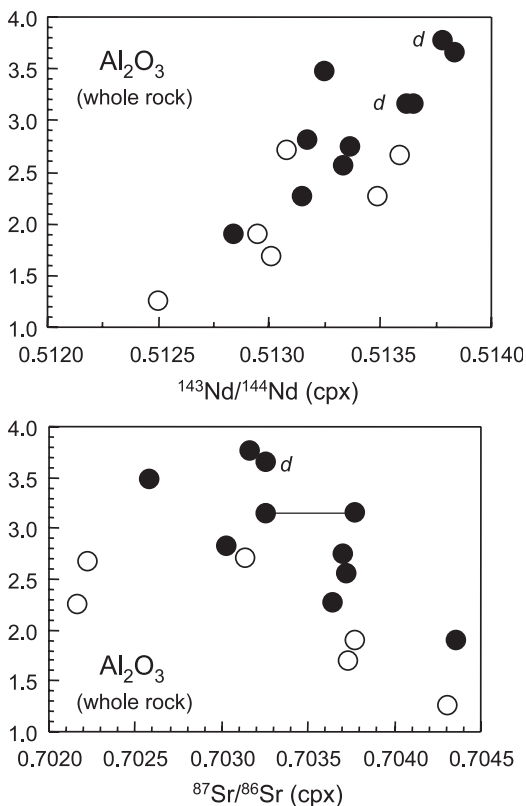


Fig. 13. Sr and Nd isotopes measured in clinopyroxene vs. whole rock Al_2O_3 concentration. Duplicate analyses are connected by tie-lines or labeled with "d". The most fertile and least metasomatized peridotites have the highest $^{143}Nd/^{144}Nd$ and lowest $^{87}Sr/^{86}Sr$. ● are data from Table 10; ○ are data from Song and Frey (1989).

some unradiogenic Nd (along with radiogenic Sr?) being introduced during alteration or recent metasomatism. The unradiogenic Nd isotopic composition of clinopyroxene leachates measured by Song and Frey (1989) supports this interpretation. However, one of our samples (DMP-19) contains clinopyroxene that is *less* radiogenic in Nd than the whole rock (Fig. 10). This sample does not exhibit REE zoning in the clinopyroxene and mass balance using the clinopyroxene mode (Table 11), which shows that the clinopyroxene accounts for all of whole rock Nd (Nd mass balances to within 2%). This mass balance makes it difficult to argue for an additional REE-bearing phase being present in the rock. The reason for the discrepancy between the Nd isotopic composition of the clinopyroxene and whole rock is not known, but it may also indicate isotopically heterogeneous clinopyroxene. Peridotites with U-shaped REE patterns or anomalously-enriched La and Ce (DMP-60) show the greatest discrepancy in Nd mass balance and/or greatest discrepancy in Nd isotopic composition between clinopyroxene and whole rock. For the other LREE-enriched peridotites (Fig. 5, lower right panel), we have no clinopyroxene data. The correspondence between LREE-enrichment and Nd isotopic heterogeneity is consistent with the lack of correlation between LREE concentration and other parameters of melt depletion (e.g., Al_2O_3) and suggests that LREE and Sr have been introduced to the peridotite after partial melting.

7.3. The timing of metasomatic overprinting

The Hannuoba peridotites experienced overprinting of the highly incompatible trace elements following melt depletion, with the most refractory samples showing the strongest overprint, as reflected in the LREE/HREE ratios (Fig. 6). Such systematics were noted long ago for peridotites from SE Australia (Frey and Green, 1974) and appear to be the norm worldwide, but are not fully understood (e.g., McDonough and Frey, 1989 and references therein). What constraints, if any, can be placed on the timing of this metasomatic overprinting?

The LREE zoning observed in two of the Hannuoba clinopyroxenes and the discrepancy between Nd isotopes in clinopyroxene vs. whole rocks reflects a lack of equilibrium in the LREE that will dissipate over time

due to diffusion. However, diffusivity of La in clinopyroxene at the temperatures of Hannuoba xenolith equilibration is quite slow: $\sim 10^{-24} \text{ m}^2 \text{ s}^{-1}$ at 1000 °C, extrapolated from data of Van Orman et al. (2001). This diffusion coefficient predicts that such LREE zoning may persist on a several millimeter scale for more than seven billion years at these temperatures. In contrast, Sr diffusivity is considerably faster. Using the data of Sneeringer et al. (1984) for Sr diffusion in clinopyroxene (10^{-19} to $10^{-21} \text{ m}^2 \text{ s}^{-1}$, extrapolated to 1000 °C) we calculate that the observed zoning will be obliterated within 30 Myr. These results suggest that the addition of LILE-rich material occurred during the Tertiary beneath Hannuoba.

Further constraints on the timing of metasomatism may be had from the correlation between Sr and Nd isotope composition and whole rock composition. These correlations (Fig. 13) can be interpreted in two ways: (1) ancient melt depletion (at 1.9 Ga from Os) followed shortly thereafter (i.e., in the Proterozoic) by variable LILE metasomatism, or (2) ancient melt depletion followed by recent metasomatism by a fluid or melt having an evolved isotopic signature. The first explanation is consistent with the positive correlation on the Nd isochron plot (Fig. 11), which yields a Proterozoic “errorchron”. In this scenario, the LREE depleted samples grow progressively more radiogenic relative to LREE enriched samples. In contrast, there is no correlation between Rb/Sr and $^{87}\text{Sr}/^{86}\text{Sr}$, therefore, the variation in $^{87}\text{Sr}/^{86}\text{Sr}$ is not due to ^{87}Sr ingrowth since the Proterozoic, and we therefore view the first alternative as unlikely.

In the second hypothesis, the metasomatic overprinting occurred recently (probably Mesozoic or younger) because the variable Sm/Nd in the peridotites would cause the trend in Fig. 13 to disappear over time due to radioactive in-growth (a similar correlation between major element composition, and Sr and Nd isotopic data with similar chronological implications was observed in lower crustal xenoliths from north Queensland, Australia; Rudnick et al., 1986). A rough positive correlation between $1/\text{Nd}$ and $^{143}\text{Nd}/^{144}\text{Nd}$ supports this mixing hypothesis. However, a similar (negative) correlation does not exist for $1/\text{Sr}$ vs. $^{87}\text{Sr}/^{86}\text{Sr}$, suggesting that additional processes may have affected the Sr isotopic composition. The scatter on the Sr–Nd isotope plot (Fig. 11) also

suggests that Sr has been affected by additional processes. If the mixing hypothesis is correct, the metasomatic agents had a maximum $^{143}\text{Nd}/^{144}\text{Nd}$ of 0.51250 ($\epsilon_{\text{Nd}} = -3$) and a minimum $^{87}\text{Sr}/^{86}\text{Sr}$ of 0.7045 (based on the most evolved isotopic compositions observed in the Hannuoba clinopyroxenes). Such isotopic compositions are more evolved than any of the Hannuoba basalts (Song et al., 1990; Tatsumoto et al., 1992), and therefore, the metasomatism likely predates this episode of magmatism.

8. Conclusions

The data presented here, coupled with the previously published Os isotopic results for these same samples provide insights into the nature of the mantle lithosphere underlying the North China craton. The main conclusions are:

- (1) The spinel peridotite xenolith suites from Hannuoba and Qixia are compositionally indistinguishable from each other and yet markedly different from cratonic mantle lithosphere found beneath other Archean cratons.
- (2) The lithospheric mantle beneath Hannuoba and Qixia formed by the loss of zero to ~25% partial melt from a primitive mantle source.
- (3) Hannuoba peridotites are melt residues formed during the Paleoproterozoic (~1.9 Ga) and Qixia peridotites are melt residues formed during the Phanerozoic (probably Mesozoic; Gao et al., 2002). Thus, there is no indication that Proterozoic lithosphere is chemically distinct from Phanerozoic lithosphere (cf., Griffin et al., 1999; O'Reilly et al., 2001).
- (4) Qixia peridotite xenoliths equilibrated over a narrower temperature interval than the Hannuoba peridotites, and the latter suite persists into the garnet stability field. This is consistent with derivation of the highest temperature Hannuoba xenoliths from greater depths.
- (5) Neither suite shows a correlation between equilibration temperature and major element composition. Thus, there is no evidence for chemical stratification of the lithosphere as might be expected if the samples formed from a simple single upwelling column of mantle.
- (6) Sr and Nd isotopic compositions of clinopyroxenes separated from Hannuoba peridotites correlate with bulk rock composition: the more refractory the sample, the more evolved the isotopic composition (Song and Frey, 1989). This, coupled with a lack of correlation between Rb/Sr and $^{87}\text{Sr}/^{86}\text{Sr}$, suggests that the peridotites are the product of recent mixing (Mesozoic or younger) between a Proterozoic lithospheric mantle with high ϵ_{Nd} (up to +23) and low $^{87}\text{Sr}/^{86}\text{Sr}$ and a metasomatic component with low ϵ_{Nd} (< -2) and higher $^{87}\text{Sr}/^{86}\text{Sr}$. The latter is significantly more evolved than the Hannuoba host basalts. Sr enrichment on clinopyroxene rims also reflects a very recent (Cenozoic) introduction of incompatible trace element-rich melts.

Acknowledgements

We thank Mike Rhodes for providing some of the XRF whole rock analyses. David Lange and Phil Piccoli provided guidance in electron microprobe analyses. Trisha Fiore helped with electron microprobe analyses at Harvard and Xiao-min Liu with XRF and ICP-MS analyses in Xi'an. We thank Stephanie Schmidberger and an anonymous reviewer for very helpful comments. The EPMA used in this study at the University of Maryland was purchased with grants from Department of Defense-Army/ARO (DAAG 559710383) and NSF (EAR-9810244), and UMD funding. This work was also supported by N.S.F. grant EAR99031591 and Nature Science Foundation of China grants 40133020 and 40373013 as well as Chinese Ministry of Science and Technology (grant G1999043202).

References

- Bennett, V.C., DePaolo, D.J., 1987. Proterozoic crustal history of the western United States as determined by neodymium isotopic mapping. *Geological Society of America Bulletin* 99, 674–685.
- Bernstein, S., Kelemen, P.B., Brooks, C.K., 1998. Depleted spinel harzburgite xenoliths in Tertiary dykes from east Greenland: restites from high degree melting. *Earth and Planetary Science Letters* 154, 221–235.
- Boyd, F.R., 1989. Compositional distinction between oceanic and cratonic lithosphere. *Earth and Planetary Science Letters* 96, 15–26.

- Brey, G.P., Köhler, T., 1990. Geothermobarometry in four-phase lherzolites: II. New thermobarometers, and practical assessment of existing thermobarometers. *Journal of Petrology* 31, 1353–1378.
- Cao, R.L., Zhu, S.-H., 1987. Mantle xenoliths and alkali-rich host rocks in eastern China. In: Nixon, P.H. (Ed.), *Mantle Xenoliths*. Wiley, Chichester, pp. 167–180.
- Chen, S., O'Reilly, S.Y., Zhou, X., Griffin, W.L., Zhang, G., Sun, M., Feng, J., Zhang, M., 2001. Thermal and petrological structure of the lithosphere beneath Hannuoba, Sino–Korean craton, China: evidence from xenoliths. *Lithos* 56, 267–301.
- Fan, Q.C., Hooper, P.R., 1989. The mineral chemistry of ultramafic xenoliths of Eastern China—implications for upper mantle composition and the paleogeotherms. *Journal of Petrology* 30, 1117–1158.
- Fan, Q.C., Liu, R.X., Li, H.M., Li, N., Sui, J.L., Lin, Z.R., 1998. Zircon geochronology and rare earth element geochemistry of granulite xenoliths from Hannuoba. *Chinese Science Bulletin* 43, 133–137 (in Chinese).
- Fan, W.M., Zhang, H.F., Baker, J., Jarvis, K.E., Mason, P.R.D., Menzies, M.A., 2000. On and off the North China craton: where is the Archaean keel? *Journal of Petrology* 41, 933–950.
- Frey, F.A., Green, D.H., 1974. The mineralogy, geochemistry and origin of lherzolite inclusions in Victorian basanites. *Geochimica et Cosmochimica Acta* 38, 1023–1059.
- Gao, S., Kern, H., Liu, Y.S., Jin, S.Y., Popp, T., Jin, Z.M., Feng, J.L., Sun, M., Zhao, Z.B., 2000. Measured and calculated seismic velocities and densities for granulites from xenolith occurrences and adjacent exposed lower crustal sections: a comparative study from the North China craton. *Journal of Geophysical Research, [Solid Earth]* 105 (B8), 18965–18976.
- Gao, S., Rudnick, R.L., Carlson, R.W., McDonough, W.F., Liu, Y., 2002. Re–Os evidence for replacement of ancient mantle lithosphere beneath the North China craton. *Earth and Planetary Science Letters* 198, 307–322.
- Govindaraju, K., 1994. 1994 compilation of working values and sample description for 383 geostandards. *Geostandards Newsletter* 18, 1–158.
- Griffin, W.L., Zhang, A.D., O'Reilly, S.Y., Ryan, C.G., 1998. Phanerozoic evolution of the lithosphere beneath the Sino–Korean craton. In: Flower, M., Chung, S.-L., Lo, C.-H., Lee, T.-Y. (Eds.), *Mantle Dynamics and Plate Interactions in East Asia*. American Geophysical Union, Washington, DC, pp. 107–126.
- Griffin, W.L., O'Reilly, S.Y., Ryan, C.G., 1999. The composition and origin of sub-continental lithospheric mantle. In: Fei, Y., Bertka, M., Mysen, B.O. (Eds.), *Mantle Petrology: Field Observations and High-Pressure Experimentation. A Tribute to France R. (Joe) Boyd*. Spec. Publ.-Geochemical Society, pp. 13–46. Houston, TX.
- Hermann, W., Berry, R.F., 2002. MINSQ—a least squares spreadsheet method for calculating mineral proportions from whole rock major element analyses. *Geochemistry: Exploration, Environment, Analysis* 2, 361–368.
- Hirth, G., Evans, R.L., Chave, A.D., 2000. Comparison of continental and oceanic mantle electrical conductivity: is the Archaean lithosphere dry? *Geochemistry, Geophysics, Geosystems* 1 2000GC000048.
- Hu, S., He, L., Wang, J., 2000. Heat flow in the continental area of China: a new data set. *Earth and Planetary Science Letters* 179, 407–419.
- Jordan, T.H., 1975. The continental tectosphere. *Reviews of Geophysics and Space Physics* 13, 1–12.
- Jordan, T.H., 1988. Structure and formation of the continental lithosphere. In: Menzies, M.A., Cox, K. (Eds.), *Oceanic and Continental Lithosphere: Similarities and Differences*. *J. Petrol.*, pp. 11–37. Special Lithosphere Issue.
- Kern, H., Gao, S., Liu, Q.-S., 1996. Seismic properties and densities of middle and lower crustal rocks exposed along the North China geoscience transect. *Earth and Planetary Science Letters* 139, 439–455.
- Kröner, A., Compston, W., Zhang, G., Guo, A., Cui, W., 1987. Single grain zircon ages for Archean rocks from Henan, Hebei and Inner Mongolia, China and tectonic implications. *Int. Symp. Tectonic Evolution and Dynamics of Continental Lithosphere*. Abst.
- Kröner, A., Compston, W., Zhang, G.W., Guo, A.L., Todt, W., 1988. Ages and tectonic setting of Late Archean greenstone–gneiss terrain in Henan Province, China as revealed by single-grain zircon dating. *Geology* 16, 211–215.
- Kusky, T.M., Li, J.-H., Tucker, R.D., 2001. The Archean Dongwanzhi Ophiolite Complex, North China craton: 2.505-billion-year-old oceanic crust and mantle. *Science* 292, 1142–1145.
- Lee, C.-T., Rudnick, R.L., 1999. Compositionally stratified cratonic lithosphere: petrology and geochemistry of peridotite xenoliths from the Labait volcano, Tanzania. In: Gurney, J.J., Gurney, J.L., Pascoe, M.D., Richardson, S.R. (Eds.), *The P.H. Nixon Volume. Proceedings VIIIth International Kimberlite Conference*. Red Roof Design, Cape Town, pp. 503–521.
- Lee, C.-T., Yin, Q., Rudnick, R.L., Jacobsen, S.B., 2001. Preservation of ancient and fertile lithospheric mantle beneath the southwestern United States. *Nature* 411, 69–73.
- Lehnert, K., Su, Y., Langmuir, C.H., Sarbas, B., Nohl, U., 2000. A global geochemical database structure for rocks. *Geochemistry, Geophysics, Geosystems-G 3 1* (Paper number 1999GC000026).
- Li, J.H., Qian, X.L., Huang, X.N., Liu, S.W., 2000. Tectonic framework of the North China craton and its cratonization in the early Precambrian. *Acta Petroli Sinica* 16, 1–10 (in Chinese).
- Liu, Y.S., Gao, S., Jin, S.Y., Hu, S.H., Sun, M., Zhao, Z.B., Feng, J.L., 2001. Geochemistry of lower crustal xenoliths from Neogene Hannuoba Basalt, North China craton: implications for petrogenesis and lower crustal composition. *Geochimica et Cosmochimica Acta* 65, 2589–2604.
- Liu, Y.S., Yuan, H.L., Gao, S., Hu, Z.C., Wang, X.C., Liu, X.M., Ling, W.-L., 2004. Zircon U–Pb geochronology of Hannuoba olivine pyroxenites: linking the 157–97 Ma basaltic underplating and granulite-facies metamorphism. *Chinese Science Bulletin* (in press).
- McDonough, W.F., Frey, F.A., 1989. Rare earth elements in upper mantle rocks. In: Lipin, B.R., McKay, G.A. (Eds.), *Geochemistry and Mineralogy of Rare Earth Elements*. Reviews in Mineralogy. Mineralogical Society of America, Washington, DC, pp. 99–145.
- McDonough, W.F., Sun, S.-S., 1995. Composition of the earth. *Chemical Geology* 120, 223–253.

- Menzies, A., Fan, W.-M., Zhang, M., 1993. Paleozoic and Cenozoic lithoprobes and the loss of >120 km of Archean lithosphere, Sino–Korean craton, China. In: Prichard, H.M., Alabaster, H.M., Harris, T., Neary, C.R. (Eds.), *Magmatic Processes and Plate Tectonics*. Geological Soc., London, pp. 71–81.
- Nimis, P., Taylor, W.R., 2000. Single clinopyroxene thermobarometry for garnet peridotites: Part I. Calibration and testing of a Cr–cpx barometer and an enstatite-in-cpx thermometer. *Contributions to Mineralogy and Petrology* 139, 541–554.
- Nyblade, A.A., Pollack, H.N., Jones, D.L., Podmore, F., Mushayandevu, M., 1990. Terrestrial heat flow in East and Southern Africa. *Journal of Geophysical Research* 95, 17371–17384.
- O'Reilly, S.Y., Griffin, W.L., Poudjom Djomani, Y.H., Morgan, P., 2001. Are lithospheres forever? Tracking changes in subcontinental lithospheric mantle through time. *GSA Today*, 4–9 (April issue).
- Pollack, H.N., 1986. Cratonization and thermal evolution of the mantle. *Earth and Planetary Science Letters* 80, 175–182.
- Qiu, Y., Groves, D.I., McNaughton, N.J., Wang, L.-G., Zhou, T., 2002. Nature, age, and tectonic setting of granitoid-hosted, orogenic gold deposits of the Jiaodong Peninsula, eastern North China craton. *China Mineral Deposita* 37, 283–305.
- Raymo, O.T., Calzia, J.P., 1998. Nd isotopic composition of cratonic rocks in the south Death Valley region: evidence for a substantial Archean source component in Mojavia. *Geology* 26, 891–894.
- Rhodes, J.M., 1996. Geochemical stratigraphy of lava flows sampled by the Hawaiian scientific drilling project. *Journal of Geophysical Research* 101, 11726–11746.
- Rudnick, R.L., McDonough, W.F., McCulloch, M.T., Taylor, S.R., 1986. Lower crustal xenoliths from Queensland, Australia: evidence for deep crustal assimilation and fractionation of continental basalts. *Geochimica et Cosmochimica Acta* 50, 1099–1115.
- Rudnick, R.L., McDonough, W.F., Orpin, A., 1994. Northern Tanzanian peridotite xenoliths: a comparison with Kaapvaal peridotites and inferences on metasomatic interactions. In: Meyer, H.O.A., Leonardos, O. (Eds.), *Kimberlites, Related Rocks and Mantle Xenoliths*. Proceedings Fifth Int. Kimb. Conf., vol. 1. CPRM, Brasilia, pp. 336–353.
- Schmidberger, S.S., Simonetti, A., Francis, D., 2003. Small-scale Sr isotope investigation of clinopyroxenes from peridotite xenoliths by laser ablation MC–ICP–MS—implications for mantle metasomatism. *Chemical Geology* 199, 317–329.
- Sneeringer, M., Hart, S.R., Shimizu, N., 1984. Strontium and samarium diffusion in diopside. *Geochimica et Cosmochimica Acta* 48, 1589–1608.
- Song, Y., Frey, F.A., 1989. Geochemistry of peridotite xenoliths in basalt from Hannuoba, Eastern China: implications for subcontinental mantle heterogeneity. *Geochimica et Cosmochimica Acta* 53, 97–113.
- Song, Y., Frey, F.A., Zhi, X.C., 1990. Isotopic characteristics of Hannuoba basalts, Eastern China—implications for their petrogenesis and the composition of subcontinental mantle. *Chemical Geology* 88, 35–52.
- Tatsumoto, M., Basu, A.R., Wankang, H., Junwen, W., Guanghong, X., 1992. Sr, Nd and Pb isotopes of ultramafic xenoliths in volcanic rocks of Eastern China: enriched components EMI and EMII in subcontinental lithosphere. *Earth and Planetary Science Letters* 113, 107–128.
- van der Hilst, R.D., McDonough, W.F. (Eds.), 1999. *Composition, Deep Structure and Evolution of Continents*. Developments in Geotectonics, vol. 24. Elsevier, Amsterdam. 342 pp.
- Van Orman, J.A., Grove, T.L., Shimizu, N., 2001. Rare earth element diffusion in diopside: influence of temperature, pressure, and ionic radius, and an elastic model for diffusion in silicates. *Contributions to Mineralogy and Petrology* 141, 687–703.
- Walter, M.J., 1999. Melting residues of fertile peridotite and the origin of cratonic lithosphere. In: Fei, Y., Bertka, M., Mysen, B.O. (Eds.), *Mantle Petrology: Field Observations and High-Pressure Experimentation*. A Tribute to France R. (Joe) Boyd. Spec. Publ.-Geochemical Society, pp. 225–240. Houston, TX.
- Wells, P.R.A., 1977. Pyroxene thermometry in simple and complex systems. *Contributions to Mineralogy and Petrology* 62, 129–139.
- White, W.M., Patchett, P.J., 1984. Hf–Nd–Sr isotopes and incompatible element abundances in island arcs: implications for magma origins and crust–mantle evolution. *Earth and Planetary Science Letters* 67, 167–185.
- Wilde, S.A., Zhou, X.H., Nemchin, A.A., Sun, M., 2003. Mesozoic crust–mantle interaction beneath the North China craton: a consequence of the dispersal of Gondwanaland and accretion of Asia. *Geology* 31, 817–820.
- Wooden, J.L., Miller, D.M., 1990. Chronologic and isotopic framework for early Proterozoic crustal evolution in the eastern Mojave Desert region, SE California. *Journal of Geophysical Research*, [Solid Earth and Planets] 95, 20133–20146.
- Wu, J.S., Geng, Y.S., Shen, Q.H., Wan, Y.S., Liu, D.Y., Song, B., 1998. *Archean Geology and Tectonic Evolution of the North China Craton* (in Chinese). Geological Publishing House, Beijing. 212 pp.
- Xu, Y.G., 2002. Evidence for crustal components in the mantle and constraints on crustal recycling mechanisms: pyroxenite xenoliths from Hannuoba, North China. *Chemical Geology* 182, 301–322.
- Yang, J.H., Wu, F.Y., Wilde, S.A., 2003. A review of the geodynamic setting of large-scale Late Mesozoic gold mineralization in the North China craton: an association with lithospheric thinning. *Ore Geology Reviews* 23, 125–152.
- Zhao, G.C., Cawood, P.A., Wilde, S.A., Sun, M., 2000. Metamorphism of basement rocks in the Central Zone of the North China craton: implications for Paleoproterozoic tectonic evolution. *Precambrian Research* 103, 55–88.
- Zhao, G.C., Wilde, S.A., Cawood, P.A., Sun, M., 2001. Archean blocks and their boundaries in the North China craton: lithological, geochemical, structural and *P–T* path constraints and tectonic evolution. *Precambrian Research* 107, 45–73.
- Zheng, Z., O'Reilly, S.Y., Griffin, W.L., Lu, F., Zhang, M., 1998. Nature and evolution of Cenozoic lithospheric mantle beneath Shandong Peninsula, Sino–Korean craton, eastern China. *International Geology Review* 40, 471–499.

- Zhi, X.C., Song, Y., Frey, F.A., Feng, J.L., Zhai, M.Z., 1990. Geochemistry of Hannuoba basalts, eastern China—constraints on the origin of continental alkalic and tholeiitic basalt. *Chemical Geology* 88, 1–33.
- Zhou, X.H., Sun, M., Zhang, G.H., Chen, S.H., 2002. Continental crust and lithospheric mantle interaction beneath North China: isotopic evidence from granulite xenoliths in Hannuoba, Sino–Korean craton. *Lithos* 62, 111–124.
- Zhu, B.-Q., 1998. *Theory and Applications of Isotope Systematics in Geosciences: Evolution of Continental Crust and Mantle in China* (in Chinese). Science Press, Beijing.
- Zindler, A., Jagoutz, E., 1988. Mantle cryptology. *Geochimica et Cosmochimica Acta* 52, 319–333.